Where in the world are condensed counterions?

Journal:	*Soft Matter*
Manuscript ID	SM-ART-10-2021-001494.R1
Article Type:	Paper
Date Submitted by the Author:	03-Dec-2021
Complete List of Authors:	Tang, Qishun; University of North Carolina at Chapel Hill College of Arts and Sciences, Rubinstein, Michael; Duke University, Departments of Mechanical Engineering and Materials Science, Biomedical Engineering, Chemistry and Physics

ARTICLE

Where in the world are condensed counterions?

Qishun Tang [a] and Michael Rubinstein *[b,c]

Received 00th January 20xx,
Accepted 00th January 20xx

DOI: 10.1039/x0xx00000x

A scaling model of the concentration profiles of both condensed and free counterions is presented for solutions of spherical and cylindrical charged nanoparticles of different charge valences, nanoparticle sizes, and salt concentrations. The distribution of counterions for both spherical and cylindrical charged particles in salt-free solutions is determined by the condensation parameter γ_0 defined as the ratio of nanoparticle valence Z_0 to the number of Bjerrum lengths $l_B = e^2/(\varepsilon kT)$ per nanoparticle size ($\gamma_0 = Z_0 l_B/(2r_0)$ for spherical nanoparticles with radii r_0 or $\gamma_0 = Z_0 l_B/L$ for cylindrical particles with length L), where ε is solution dielectric permittivity, e is elementary charge and kT is thermal energy. Depending on the magnitudes of the condensation parameter γ_0 and nanoparticle volume fraction ϕ, we find three qualitatively different regimes for the counterion distribution near charged particles: (i) weakly charged particles with no condensed counterions, (ii) particles with weak counterion condensation with less than half of the counterions condensed, and (iii) regime of strong counterion condensation with the majority of counterions condensed. The magnitude of electrostatic energy of a condensed counterion with respect to solution locations with zero electric field is larger than thermal energy kT, and the fraction of condensed counterions increases from less than half in the weak condensation regime to the majority of all counterions in the strong condensation regime. The condensed counterions are not bound to the nanoparticle surface but instead are localized within the condensed counterion zone near the charged particle. The thickness of the condensed counterion zone varies with the condensation parameter γ_0, the nanoparticle shape and volume fraction ϕ, and the salt concentration and can be as narrow as Bjerrum length (~nm) or as large as the particle size (~L the length of charged cylinder).

Introduction

Electrostatic stabilization is one of the main methods of preparing homogeneous solutions of colloids and polymers in polar solvents such as water. Stabilization of these solutions takes place both due to the entropy of counterions and due to the electrostatic repulsion between charged objects. Increasing the bare charge of nanoparticles or polymers does not necessarily lead to improved solution stability. Counterions to this additional charge may not be able to escape the strong electrostatic attraction and are instead localized near these highly charged surfaces reducing their effective charge.

The motion of the counterions and charged particles due to the action of the external electric field or fluid flow is also affected by the electrostatic interactions between the charged particles and their counterions. The electrophoretic mobility of charged particles or polymers is reduced by the drag imposed by the counterions pulled in the opposite direction by the external electric field. The viscosity of dilute solutions of polyelectrolytes and charged particles depends on the way counterions that are strongly electrostatically coupled to these solutes modify the solvent flow around these solutes. In all of these examples, it is essential to know the distribution of counterions around charged particles of different charge valences, shapes, sizes, and concentrations in solution as well as the strength of electrostatic interactions between these particles and their counterions.

The distribution of counterions at charged surfaces with different symmetries – planes, cylinders, and spheres has been extensively studied. In the present paper, we summarize and connect these classical results on counterion distribution and condensation at surfaces with different symmetries into a comprehensive scaling picture. The Gouy-Chapman theory[1,2] presents the analytical solution of counterion distribution near a charged plane[3,4], which will be reviewed in the introduction below for the salt-free case and used throughout the paper. The classical results[5,6] of counterion distribution near charged cylinders were obtained within the cylindrical cell model applicable to semidilute solutions containing cylinders much longer than the distance between them. This cell model was extended to dilute solutions of charged cylinders[7] with the analytical solution of the counterion distribution inside the non-electroneutral cylindrical cell. The counterion condensation on spherical particles was studied theoretically for salt-free and added-salt cases[8–12]. In the present paper, we address the following questions: 1) What simple physical concepts can be used to describe counterion condensation based on general symmetry principles? 2) How does the counterion condensation around the cylinders and spheres and the corresponding

---

[a] Department of Applied Physical Sciences, University of North Carolina, Chapel Hill, NC 27599, USA.
[b] Departments of Mechanical Engineering and Materials Science, Biomedical Engineering, Chemistry and Physics, Duke University, Durham, NC 27708. Email: michael.rubinstein@duke.edu
[c] Institute for Chemical Reaction Design and Discovery (WPI-ICReDD), Hokkaido University, Sapporo 001-0021, Japan

† Electronic Supplementary Information (ESI) available: See DOI: 10.1039/0xx00000x

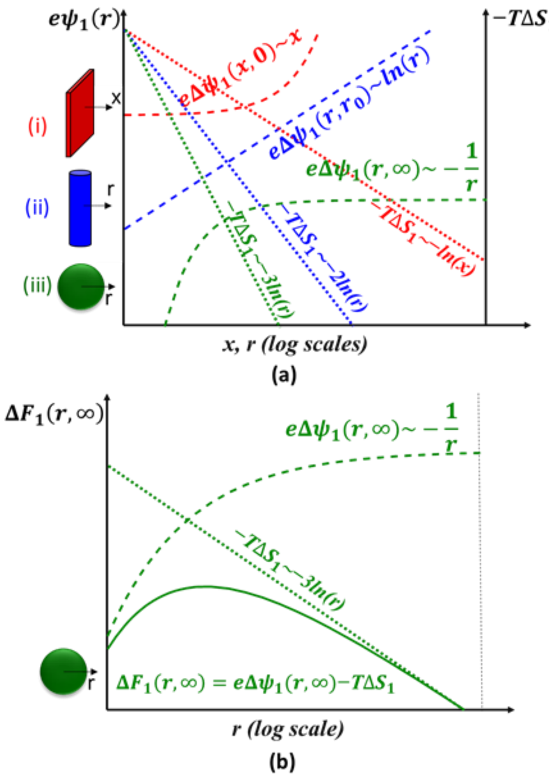

Fig. 1 (a) Electrostatic (dashed lines) and entropic (dotted line) parts of free energy of a single counterion in the electric field with (i) planar symmetry (red), (ii) cylindrical symmetry (blue), and (iii) spherical symmetry (green). Distance from the planar surface is x, while the distance from the axis of the cylinder or the center of the sphere is r. (b) Single counterion free energy (solid line) with its electrostatic (dashed line) and entropic (dotted line) parts in the electric field with spherical symmetry. A single counterion escapes from a charged particle upon sufficient dilution indicated by lower values of $\Delta F_1(r, r_{ref})$ at large r.

osmotic pressure change with the concentration and charge of particles? To address these questions, we will analyze the interplay of counterion entropy and electrostatic attraction in fields with different symmetries. In Appendix D we will address the effect of electrostatic screening by added salt on the counterion distribution.

The ability of a charged surface to attract counterions depends on both the charge density and the shape of this surface (Fig. 1(a)). The relative interplay of entropic and electrostatic parts of the counterion free energy at charged surfaces with different symmetries can be qualitatively understood based on the dependence of the electrostatic potential on the distance from the surface in the absence of counterions.

The electrostatic potential $\Delta\psi_1$ (energy of a unit probe charge) in the absence of counterions (that in real solutions modify this potential) increases linearly with distance x from a planar charged surface (eqn (1a)), logarithmically with distance r from the symmetry axis of a charged cylinder (eqn (1b)), and as -1/r – reciprocally with distance r from the center of a charged spherical nanoparticle (eqn (1c)) - see dashed lines in Fig. 1(a).

$$\Delta\psi_1(x,0)\sim x \quad \text{for charged plane} \tag{1a}$$

$$\Delta\psi_1(r,r_0)\sim \ln(r/r_0) \quad \text{for charged cylinder} \tag{1b}$$

$$\Delta\psi_1(r,\infty)\sim -1/r \quad \text{for charged sphere} \tag{1c}$$

The function $\Delta\psi_1(r, r')$ is defined as the electrostatic potential difference between radii locations r' and r for cylindrical ($r' = r_0$ in eqn (1b)) and spherical ($r' = \infty$ in eqn (1c)) particles, while for planar surfaces $\Delta\psi_1(x, 0)$ is defined as the potential difference between points with coordinate x (distance x away from the surface) and the charged surface at $x = 0$. The single counterion entropic free energy (assuming no other counterions present) decreases logarithmically with increasing exploration volume (see dotted lines in Fig. 1(a)) for all three symmetries of charged surfaces

$$-T\Delta S_1 \sim -kT\ln V \sim -DkT\ln r \tag{2}$$

where r is the linear size of volume V this single counterion is allowed to explore, and D is the dimensionality related to the symmetry of the electric field (D=1 for planar, D=2 for cylindrical, and D=3 for spherical symmetry). By comparing the variation of electrostatic $e\Delta\psi_1$ (eqn (1)) and entropic $-T\Delta S_1$ (eqn (2)) parts of the single counterion free energy ΔF_1 with distance from the charged surface in the absence of other counterions,

$$\Delta F_1 = e\Delta\psi_1 - T\Delta S_1 \tag{3}$$

We observe that for planar symmetries the linear increase of the electrostatic potential with the distance from the charged surface (eqn (1a)) is stronger than the logarithmic decrease of the entropic part of free energy (eqn (2)). This implies that a counterion will condense towards a large enough charged planar surface with the minimum of the single counterion free energy ΔF_1 near the surface (see Fig. 2(a)). For cylindrical symmetries, both functional dependences (eqns (1b) and (2)) are logarithmic and one needs to compare the coefficients in front of these logarithms to determine whether electrostatic or

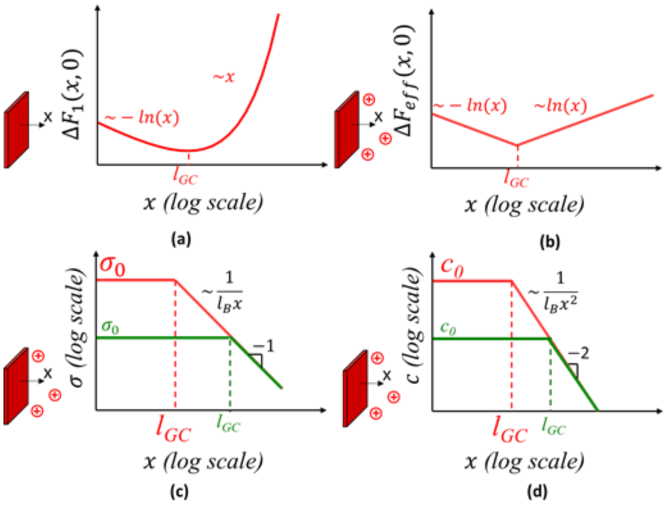

Fig. 2 (a) The single counterion free energy difference $\Delta F_1(x, 0)$ as a function of distance x from the charged planar surface (in the absence of other counterions). (b) The effective mean-field free energy difference $\Delta F_{eff}(x, 0)$ per counterion as a function of distance x from the charged planar surface in the multi-counterion case. (c) The effective surface charge number density $\sigma(x)$ and (d) the counterion concentration profile $c(x)$ as a function of distance x from the charged planar surface with bare surface charge number density σ_0 for a larger (red) and a smaller (green) value of σ_0. The effective charge and counterion concentration profile are independent of the surface charge density at distances from the charged planar surface larger than Gouy-Chapman length.

entropic part of the free energy dominates. For spherical symmetries, the logarithmic decrease of the entropic part (eqn (2)) is stronger than the increase of the electrostatic part (eqn (1c)) at a large distance from the charged surface. This implies that a counterion will be able to escape from the charged surface with a spherically symmetric electric field upon sufficient dilution of charged spherical particles (Fig. 1(b)). These three qualitatively different conclusions for the interplay of entropic and electrostatic parts of the single counterion free energies for the three different symmetries of the electric field are the main concepts extended below to the physically relevant case of more than one counterion and used for the scaling description of the counterion distribution and condensation.

In the unphysical case of a single counterion at a charged planar surface with the bare surface charge number density σ_0, its free energy $\Delta F_1(x,0)$ (Fig. 2(a)) has a minimum at length scale on the order of the Gouy-Chapman length

$$l_{GC} \approx (\sigma_0 l_B)^{-1} \tag{4}$$

where the counterion electrostatic energy difference between the surface (x=0) and distance l_{GC} away from the surface is $e\Delta\psi_1(l_{GC},0) \approx kT$. Here and below the approximately equal sign "≈" denotes scaling equality up to a numerical coefficient. k is the Boltzmann constant, T is the absolute temperature, and l_B is the Bjerrum length:

$$l_B = \frac{e^2}{\varepsilon kT} \tag{5}$$

defined as the distance at which the electrostatic interaction energy between two elementary charges in a medium with dielectric permittivity ε is equal to thermal energy kT, where e is the elementary charge.

In a much more realistic multi-counterion case, the electrostatic part of effective mean-field single counterion free energy $\Delta F_{eff}(x, x_{ref})$ is modified by other counterions (see eqn (7) below for the precise definition). For a charged planar surface, the effective charge valence is reduced by the counterions (assumed monovalent) located between the surface and the plane at a distance x from it (Fig. 2(c))

$$\sigma(x) = \sigma_0 - \int_0^x c(x')dx' \tag{6}$$

The effective single counterion mean-field free energy difference $\Delta F_{eff}(x, x_{ref})$ (see Fig. 2(b)) accounts for the actual electrostatic potential difference $\Delta\psi(x, x_{ref})$, where x_{ref} is the reference location with respect to which the electrostatic potential difference $\Delta\psi$ is measured.

$$\begin{aligned} \Delta F_{eff}\left(x, x_{ref}\right) &\approx e\Delta\psi\left(x, x_{ref}\right) - T\Delta S_1 \\ &\approx e\Delta\psi\left(x, x_{ref}\right) - DkT\ln\left(x / x_{ref}\right) \end{aligned} \tag{7}$$

The entropic part $-T\Delta S_1$ of the effective single counterion mean-field free energy changes logarithmically with exploration volume x^D with D-dimensional symmetry $\sim -DkT\ln x$ on length scale x. Since the electrostatic potential is reduced by the other counterions, the effective single counterion mean-field free energy $\Delta F_{eff}(x,0)$ increases logarithmically (Fig. 2(b)) rather than linearly (Fig. 2(a)) at distance $x > l_{GC}$ from the planar charged surface. Note that the effective single counterion mean-field free energy $\Delta F_{eff}(x, x_{ref})$ is different from the counterion chemical potential Δμ (see Table 1). For the chemical potential Δμ, the entropy of all counterions (rather than of a single counterion) is accounted for, so the entropic part of the chemical potential changes logarithmically with the counterion concentration $c(x)$ (instead of the exploration volume x^D). The counterion chemical potential is a constant independent of the location x as described by the Boltzmann equation (eqn (20)):

$$\begin{aligned} \Delta\mu &= e\Delta\psi\left(x, x_{ref}\right) - T\Delta S \\ &= e\Delta\psi\left(x, x_{ref}\right) - kT\ln\left(c(x)/c\left(x_{ref}\right)\right) = 0 \end{aligned} \tag{8}$$

Table 1 Different types of counterion free energies with their corresponding electrostatic and entropic parts.

Free energy type	Electrostatic part	Entropic part
Single counterion free energy: ΔF_1	Bare: $e\Delta\psi_1$	Single counterion: $-T\Delta S_1 \sim -DT\Delta ln r$
Effective single counterion mean-field free energy: ΔF_{eff}	Compensated by counterions: $e\Delta\psi$	Single counterion: $-T\Delta S_1 \sim -DT\Delta ln r$
Chemical potential: $\Delta\mu$	Compensated by counterions: $e\Delta\psi$	Multi-counterion: $-T\Delta S \sim -T\Delta ln c$

The different types of free energies are compared in Table 1.

The effective single counterion mean-field free energy $\Delta F_{eff}(x, x_{ref})$ is used throughout the paper to quantify the counterion population at different length scales from the charged surface, as the exponential of $-\Delta F_{eff}(x, x_{ref})/kT$ is related to the probability P(x) for a counterion (equivalent to counterion population) to be located within dx of distance x from the nanoparticle surface:

$$\begin{aligned} P(x)dx &\approx c(x)x^{D-1}dx \approx c(x)x^D d\ln x \\ &\approx \exp(-\Delta F_{eff}(x, x_{ref})/kT)d\ln x \end{aligned} \tag{9}$$

The last part of eqn (9) used Boltzmann relation between counterion concentration c(x) and electrostatic potential $\Delta\psi(x, x_{ref})$ (see eqns (7) and (20)).

The Gouy-Chapman solution[1,2] for counterion condensation near a charged planar surface in the absence of added salt is one of the main concepts underlying all counterion condensation cases. The total number of the counterions per unit area within the Gouy-Chapman length l_{GC} (eqn (4)) from the surface is on the order of the bare surface charge number density σ_0 (in order to reduce the effective charge value by a factor of 2; see eqn (11)). This implies that the counterion number density within the Gouy-Chapman length from the surface is

$$c_{GC} \approx \sigma_0 / l_{GC} \approx \left(l_B l_{GC}^2\right)^{-1} \tag{10}$$

where we used $\sigma_0 \approx (l_{GC} l_B)^{-1}$ from eqn (4). The main feature of the strong counterion condensation is that both the effective surface charge number density $\sigma(x)$ (Fig. 2(c)) and the counterion number density (concentration) profile $c(x)$ (Fig. 2(d)) are independent of the bare surface charge number density σ_0 at distances from the surface larger than l_{GC}. The effective charge number density at any distance $x > l_{GC}$ from the surface is reduced in a self-similar way so that distance x corresponds to the new Gouy-Chapman length of that effective surface charge number density at that distance, $\sigma(x) \approx (xl_B)^{-1}$

(see the overlap of green and red lines at green l_{GC} in Fig. 2(c)). The counterion number density profile $c(x)$ at distances $x > l_{GC}$ with $c(x) \approx \sigma(x)/x \approx (l_B x^2)^{-1}$ (see Fig. 2(d)) can be obtained from the counterion number density at Gouy-Chapman length $c_{GC} = c(l_{GC}) \approx \sigma_0 / l_{GC} \approx \left(l_B l_{GC}^2\right)^{-1}$ (eqn (10)) by replacing l_{GC} with x and σ_0 with the corresponding effective charge number density $\sigma(x)$. The scaling form of the analytical salt-free Gouy-Chapman solution for both effective charge number density $\sigma(x)$ and counterion concentration profile $c(x)$ in the salt-free case is:

$$\sigma(x) \approx \frac{1}{l_B}\frac{1}{x+l_{GC}} \approx \begin{cases} \sigma_0 & \text{for } x < l_{GC} \\ (l_B x)^{-1} & \text{for } x > l_{GC} \end{cases} \tag{11}$$

$$c(x) \approx \frac{\sigma(x)}{x+l_{GC}} \approx \frac{1}{l_B}\frac{1}{\left(x+l_{GC}\right)^2} \approx \begin{cases} \sigma_0^2 l_B & \text{for } x < l_{GC} \\ \left(l_B x^2\right)^{-1} & \text{for } x > l_{GC} \end{cases} \tag{12}$$

The salt-free Gouy-Chapman solution describes the distribution of counterions that are strongly attracted but not bound to the oppositely charged surface with fixed and uniformly distributed charge. Note that if the nanoparticles and solvent have different dielectric constants, one could use image charges to describe the boundary conditions for electric field at the particle surface[13]. These image charges would have an additional effect on the counterion distribution near the surface. For simplicity, we do not consider this effect by assuming the same dielectric constant of particles and solvent without any image charges. In some cases, there could be a layer of counterions bound (either chemisorbed or strongly physisorbed) to the surface, called the Stern layer[14] and the extent of binding could depend on the counterion concentration[15,16]. In addition, the Gouy-Chapman model makes the mean-field approximation and ignores the repulsion between neighboring counterions. Therefore, the model is valid if the average distance between counterions near the charged surface is larger than Bjerrum length l_B and the repulsion energy between two neighboring counterions is less than kT. This condition restricts the surface charge number density to $\sigma_0 < 2\pi l_B^{-2}$. At higher surface charge density one expects the formation of the Wigner layer[17–20] of counterions that are strongly attracted to the surface (with energy $\gg$ kT per counterion) and are strongly repelled from each other with a 2D lattice structure. For the Wigner layer to exist, the surface charge needs to be continuous, as a strong attraction to discrete surface charges would lead to counterion binding. In the present paper, we do not consider either Stern or Wigner layers and assume that the bare surface charge density $\sigma_0 < 2\pi l_B^{-2}$ is already reduced from the original surface charge density by the charge density of the counterions in Stern and/or Wigner layers if these layers exist. Outside of these layers, there could still be condensed counterions with the electrostatic energy difference between locations close to and far from charged objects larger than thermal energy kT. One of the objectives of the present paper is to describe the distribution of these condensed counterions as well as that of the "free" counterions that dominate the osmotic pressure of these solutions. The understanding of the distribution of counterions that are condensed but not bound to the charged surface is important for electrophoretic mobility of charged particles and polymers, viscosity of their solutions as well for understanding of the ion exchange membranes[21].

The counterion condensation is also affected by the presence of salt. In a solution containing added salt, the electrostatic field is not only reduced by the condensed counterions but is also screened by salt ions on length scales larger than the Debye length[22]:

$$r_D \approx \left(l_B c_s\right)^{-1/2} \tag{13}$$

Most of the counterions dissociated from the nanoparticles and extra salt ions with the sign opposite to the nanoparticle charge are localized within the Debye length r_D and significantly compensate the nanoparticle charge. Outside the Debye length r_D, the electrostatic field decays exponentially with distance x from the charged surface $\sim\exp(-x/r_D)$. In this paper, we focus on the low salt solutions with the average distance between solute particles smaller than the Debye length. The effect of salt on counterion distribution is discussed in Appendix D. The solutions of charged spherical nanoparticles (NPs) are analyzed in Section 2, while counterion distribution in solutions of cylindrical nanoparticles is presented in Section 3. The nanoparticle concentration and the condensation parameter dependence of osmotic pressure in solutions of charged particles is discussed in Section 4. The main ideas of the paper including the length scales important for counterion distribution are summarized in Section 5.

2. Solutions of charged spherical nanoparticles

In this section, we describe the counterion distributions around spherical nanoparticles. We consider spherical particles with bare charge valence Z_0 and radius r_0 (see Fig. 3). The bare surface charge number density is:

$$\sigma_0 = \frac{Z_0}{4\pi r_0^2} \quad \text{spherical NPs} \tag{14}$$

We define the normalized charge line number density - called the condensation parameter γ_0: the number of elementary charges times the Bjerrum length l_B and divided by the largest dimension of the nanoparticle ($2r_0$ for spheres).

$$\gamma_0 = \frac{Z_0 l_B}{2r_0} = 2\pi\sigma_0 r_0 l_B \quad \text{spherical NPs} \tag{15}$$

Charged nanoparticles are dissolved in a polar solvent at a dilute concentration corresponding to the average distance of $2r_{cm}$ between centers of neighboring particles. The volume fraction is defined as the ratio of the physical volume occupied by all particles to the total volume of the solution. The volume fraction is the product of the physical volume and the number density of nanoparticles. The physical volume of a spherical particle is $\sim r_0^3$, while their number density is $\sim r_{cm}^{-3}$. Therefore volume fraction ϕ of spherical nanoparticles is:

$$\phi \approx r_0^3 / r_{cm}^3 \quad \text{spherical NPs} \tag{16}$$

The electric field $\vec{E}(r)$ around a charged nanoparticle can be calculated using Gauss's law:

$$\left| \oiint_S \vec{E}(r) \cdot dA \right| \approx \frac{eZ(r)}{\varepsilon} \tag{17}$$

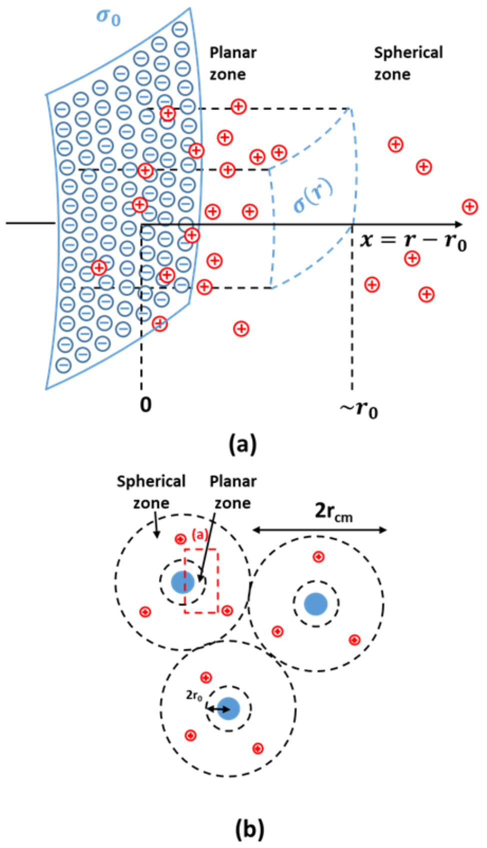

Fig. 3 Solution of negatively charged spherical particles. The interaction between the charged surface and counterions can be approximately described within two different symmetry zones: (a) planar symmetry zone for $x = r - r_0 < r_0$; (b) spherical symmetry zone for $r_0 < x < r_{cm}$.

where $Z(r)$ is the effective valence of the nanoparticle as viewed from distance r (that includes the nanoparticle valence and all counterions up to distance r). Based on Gauss's law, the electric field strength decreases with increasing distance r away from the charged nanoparticle not only due to a larger surface enclosing the particle but also because of the increasing number of enclosed counterions compensating the bare charge and decreasing the effective valence $Z(r)$ of the particles.

The electric field near a charged nanoparticle can be approximated by planar symmetry very close to the smooth nanoparticle surface ($0 < x = r - r_0 \ll r_0$, Fig. 3(a))

$$\left|\vec{E}(x)\right| \approx \frac{e\sigma(x)}{\varepsilon},\ \sigma(x) = \sigma_0 - \int_0^x c(x')dx' \qquad (18)$$

planar symmetry zone: $r - r_0 \ll r_0$

Electric field far away from particles in dilute solution has spherical symmetry at distances larger than the nanoparticle size (for spherical nanoparticle the field is spherical everywhere, but we define spherical zone to be generalizable to particles of other shapes as: $r_0 < x = r - r_0 < r_{cm}$, Fig. 3(b)).

$$\left|\vec{E}(r)\right| \approx \frac{eZ(r)}{\varepsilon r^2},\ Z(r) = Z_0 - 4\pi\int_{r_0}^{r} c(r')r'^2 dr' \qquad (19)$$

spherical symmetry zone: $r_0 < r - r_0 < r_{cm}$

The electric field $E(r)$ is the rate of change of the electrostatic potential $\Delta\psi(r, r_{cm})$ that controls the counterion

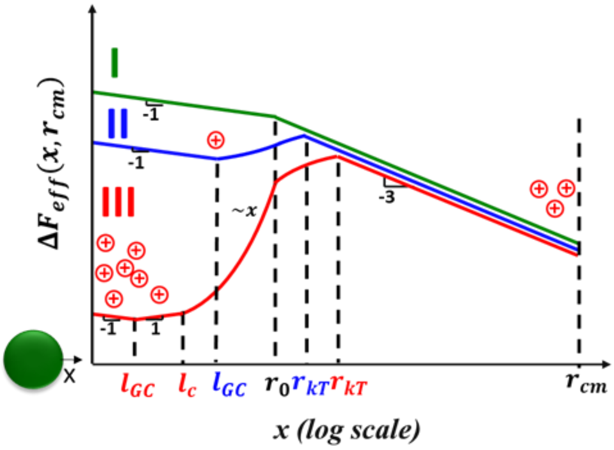

Fig. 4 The three regimes of the dependence of the effective single counterion mean-field free energy on the distance from the spherical nanoparticle surface: I. Weakly charged (green line); II. Weak counterion condensation (blue line); and III. Strong counterion condensation (red line).

concentration profile $c(r)$ through Boltzmann distribution assuming positive monovalent counterions:

$$c(r) \approx c(r_{cm})\exp\left(-\frac{e\Delta\psi(r, r_{cm})}{kT}\right) \qquad (20)$$

Note that the electrostatic potential in solutions with many counterions between particles differs from the simple expressions presented in eqn (1) and sketched in Fig. 1(a) for the case of no other counterions in solution, as counterions surrounding charged particles modify the electric field profile (see eqns (18) and (19)). Nevertheless, the qualitative analysis can be performed in a similar way, but with electrostatic potential accounting for all ions in the solution. The probability for a counterion to be at location x is controlled by the effective

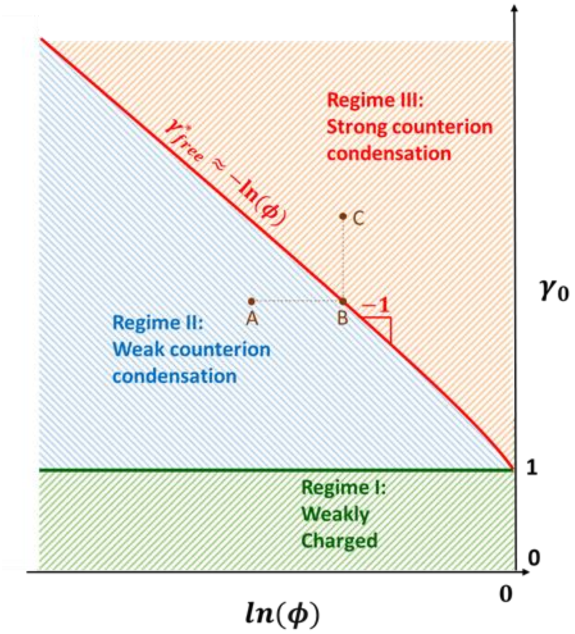

Fig. 5 Schematic diagram of the counterion regimes for charged spherical particles. Regime I: weakly charged particles (no counterion condensation); regime II: weak counterion condensation; regime III: strong counterion condensation. Condensation parameter for spherical nanoparticles $\gamma_0 = Z_0 l_B/(2r_0)$ is the nanoparticle valence Z_0 normalized by the number of Bjerrum lengths l_B per nanoparticle size.

single counterion mean-field free energy $\Delta F_{eff}(x, r_{cm})$ (eqns (7) and (9)). Depending on the fraction of condensed counterions (see Fig. 4), we define three different regimes for the counterion distribution:

I. Weakly charged particles with no condensed counterions: the magnitude of electrostatic energy of all counterions with respect to locations with zero electric field (outer boundary of the spherical zone $r \approx r_{cm}$) is less than thermal energy kT. The effective single counterion potential $\Delta F_{eff}(x, r_{cm})$ for weakly charged nanoparticles is monotonically decreasing with distance x from the particle surface (green line in Fig. 4). This effective potential has only one minimum at large distances $x \sim r_{cm}$ corresponding to free counterions.

II. Weak counterion condensation with less than half of all counterions condensed at condensation parameter $\gamma_0 > 1$ (see eqn (15) for the definition of the condensation parameter) and high dilution – low volume fraction ϕ. The effective single counterion potential $\Delta F_{eff}(x, r_{cm})$ has two minima (blue line in Fig. 4). The majority of counterions are free and are far from the charged particle surface with the entropic part of their free energy dominating $\Delta F_{eff}(x, r_{cm})$. The smaller fraction of counterions are condensed in the shallower minimum of $\Delta F_{eff}(x, r_{cm})$ near the charged surface. The magnitude of the electrostatic energy of these condensed counterions is larger than thermal energy $|e\Delta\psi(x, r_{cm})| > kT$.

III. Strong counterion condensation. At higher condensation parameter γ_0 and volume fraction ϕ, the majority of the counterions are condensed in the minimum of $\Delta F_{eff}(x, r_{cm})$ at small $x \sim l_{GC}$ near the nanoparticle surface (red line in Fig. 4).

The three different counterion condensation regimes are shown in the diagrams of states for solutions of charged spherical particles (Fig. 5) characterized by two dimensionless parameters: the condensation parameter γ_0 - the normalized charge line number density of the particles (eqn (15)) and the volume fraction ϕ of nanoparticles (eqn (16)). The examples of parameters for each regime are shown in Appendix A.

Below we discuss the counterion distribution of the corresponding regimes of spherical charged particles (Fig. 5).

Regime I. Weakly charged particles ($\gamma_0 < 1$). In this regime, the majority of counterions are far from the weakly charged nanoparticle surface. The bare charge valence of weakly charged particles is not significantly compensated by the counterions at any length scale up to the distance between nanoparticles. This means that the effective charge valence does not change much with distance $Z(r) \approx Z_0$ up to length scales $r \sim r_{cm}$ (see the horizontal part of the green line in Fig. 6(a)) and the electrostatic potential can be approximated by that due to the bare charge valence Z_0 (see Fig. 1(aiii)). The counterion concentration does not significantly vary with distance $x = r - r_0$ from the nanoparticle surface in the planar zone because the Gouy-Chapman length is larger than the thickness of the planar zone ($l_{GC} \approx (\sigma_0 l_B)^{-1} \approx r_0/\gamma_0 > r_0$). In the spherical zone, almost all counterions are free and distributed almost uniformly, because the difference of counterion electrostatic energy between inner and outer boundaries of the spherical zone is smaller than kT ($|e\Delta\psi(r_0, r_{cm})| = \gamma_0 kT < kT$). The counterion concentration changes by less than the factor of $e \cong 2.7$ since $Z_0 l_B/r < \gamma_0 < 1$ in the spherical zone (see green line for $x > r_0$ in Fig. 6(b)):

$$c(r) \approx \frac{Z_0}{r_{cm}{}^3} \exp\left(\frac{Z_0 l_B}{r}\right) \approx \frac{Z_0}{r_{cm}{}^3}\left(1 + \frac{Z_0 l_B}{r}\right) \quad (21)$$

in the spherical zone ($r > 2r_0$) in regime I

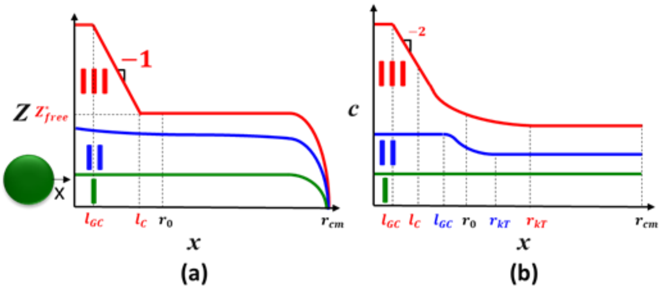

Fig. 6 Scaling description of counterion distribution profiles for charged spheres: (a) Effective charge valence $Z(x)$ as a function of the distance from the nanoparticle surface $x = r - r_0$. (b) Counterion concentration $c(x)$ as a function of the distance from the surface $x = r - r_0$. Weakly charged particles regime I (green), weak counterion condensation regime II (blue), and strong counterion condensation regime III (red). All axes are logarithmic. The scaling dependence is compared to the numerical solution from the nonlinear Poisson Boltzmann (eqn (19) and (20)) in Appendix B.

We define the free zone as the region of space with the magnitude of counterion electrostatic energy less than kT so that the magnitude of the electrostatic energy of a counterion at the inner boundary of the free zone r_{kT} with respect to the outer boundary r_{cm} is equal to the thermal energy ($|e\Delta\psi(r_{kT}, r_{cm})| = kT$). Here and below the magnitude of the electrostatic potential means the absolute value of the electrostatic potential relative to that at the boundary between neighboring particles – location with zero electric field. Thus, the entire solution in regime I is the free zone with no condensed counterions.

Regime II. Weak counterion condensation regime ($1 < \gamma_0 < \gamma^*_{free}(\phi)$). In this regime, the variation of the counterion electrostatic energy across the spherical zone is larger than kT ($|e\Delta\psi(r_0, r_{cm})| \approx \gamma_0 kT > kT$). The strong electrostrostaic attraction to the particle causes localization (condensation) of some counterions near the charged surface. In regime II, the volume fraction of nanoparticles ϕ is still low enough resulting in the majority of counterions being free to explore solution volume far from the particle surface (see blue line in Fig. 4). The counterion concentration near the nanoparticle surface $c(r_0)$ is still lower than the Gouy-Chapman concentration $c_{GC} \approx \sigma_0^2 l_B \approx \gamma_0^2/(l_B r_0^2)$ (eqns (10) and (15)). More than half of all counterions are in the free zone - further away from the nanoparticle than r_{kT} ($Z_{free} > Z_0/2$) with the free charge valence Z_{free} defined as the charge valence not compensated by the condensed counterions. Correspondingly, less than half of all counterions are condensed (localized near the nanoparticle surface) $Z_{cond} = Z_0 - Z_{free} < Z_0/2$. Therefore, this regime is called “weak counterion condensation”. The electrostatic energy of a counterion at location r in regime II can be estimated (similar to regime I) by the electrostatic potential of the bare nanoparticle charge $|e\Delta\psi(r, r_{cm})|/kT \approx Z_{free} l_B/r \approx Z_0 l_B/r$ (eqn (1c) in the spherical zone) because this charge is reduced by condensed counterions by less than a factor of two in the weak counterion condensation regime. The free counterions are almost uniformly distributed in the free zone $x > r_{kT}$ with the location of the inner boundary of the free zone at $r_{kT} \approx Z_{free} l_B \approx Z_0 l_B$ and the effective charge valence of a nanoparticle is approximately equal to its bare valence $Z(r) > Z_0/2$ for almost all distance r on logarithmic scale except very close to the outer boundary of the spherical zone r_{cm} where $Z(r)$ decays to zero (see blue line in Fig. 6(a)). The condensed counterions are localized within a narrow zone of thickness l_c near the charged surface, called the condensed counterion zone. In the weak counterion condensation regime, the thickness of the condensed counterion zone l_c is the Gouy-Chapman length $l_{GC} \approx (\sigma_0 l_B)^{-1} \approx r_0/\gamma_0$ (eqns (4) and (15)). The difference of the counterion electrostatic energy between any point within the condensed counterion zone and the nanoparticle surface is less than thermal energy kT in this weak condensation regime. Between the condensed counterion zone and the free zone ($l_c < x < r_{kT}$), there is a zone with a large counterion concentration variation but a small fraction of counterions located there. Such spatial regions are called “empty” zones. The empty zone in regime II is between $l_c \approx l_{GC}$ and $r_{kT} \approx Z_0 l_B$ characterized by the almost constant effective charge $Z(r)$ (blue line in Fig. 6(a)) but strongly varying counterion concentration $c(r)$ (blue line in Fig. 6(b)). The strong variation of the counterion concentration is due to the sharp decrease of the magnitude of electrostatic potential $|e\Delta\psi(r, r_{cm})| \approx kTZ_0 l_B/(r_0 + x)$ with distance x from the particle surface in this empty zone (eqn (20)). The change of the electrostatic potential dominates over the change of entropic part of free energy in the empty zone leading to the higher value of effective single counterion mean-field free energy $\Delta F_{eff}(x, r_{cm})$, which forms the free energy barrier between the two minima (see $l_{GC} < x < r_{kT}$ part of the blue line in Fig. 4). The higher value of effective single counterion mean-field free energy $\Delta F_{eff}(x, r_{cm})$ prevents counterions from being located in the empty zone. The electrostatic potential gradually saturates in the free zone, ($x > r_{kT} \approx Z_0 l_B$) resulting in the almost constant counterion concentration there $c(r) \approx c_{free} \approx Z_0/r_{cm}^3$ (varies by less than factor e). The effective single counterion mean-field free energy is dominated in the free zone by the change of the entropic part of free energy, which decreases logarithmically with distance from the particle $\Delta F_{eff}(x, r_{cm}) \sim -3kT\ln(x/r_{cm})$ (see $x > r_{kT}$ part of blue line in Fig. 4). The resulting relatively low value of the effective single counterion mean-field free energy with the minimum at r_{cm} traps the majority of the counterions. Thus in the weak condensation regime, the majority of counterions are free in the free zone ($r_{kT} < x < r_{cm}$), a small fraction of counterions are condensed in the condensed counterion zone ($x < l_{GC}$) and almost no counterions are in the empty zone ($l_{GC} < x < r_{kT}$).

$$4\pi\int_{l_{GC}}^{r_{kT}} c(x)(r_0+x)^2\,dx \ll 4\pi r_0^2\int_0^{l_{GC}} c(x)\,dx = Z_{cond}$$
$$< 4\pi\int_{r_{kT}}^{r_{cm}} c(x)(r_0+x)^2\,dx = Z_{free} \approx Z_0 \qquad (22)$$
$$\text{spherical NPs, regime II}$$

The number of condensed counterions can be estimated as the concentration at the nanoparticle surface $c(r_0)$ (eqn (20)) with surface potential $\Delta\psi(r_0, r_{cm}) \approx -kT\gamma_0/e$ times the volume of a layer with the thickness of Gouy-Chapman length l_{GC} around the nanoparticle (NP).

$$Z_{cond} \approx c(r_0) l_{GC} r_0^2 \approx \frac{r_0^4}{r_{cm}^3 l_B}\exp(\gamma_0) \quad \text{spherical NPs, regime II} \qquad (23)$$

At the upper boundary of the weak counterion condensation regime, the concentration of condensed counterions at the nanoparticle surface $c(r_0)$ reaches the Gouy-Chapman concentration $c_{GC} \approx \gamma_0^2/(l_B r_0^2)$ (eqns (10) and (15)). At this crossover between weak and strong condensation regimes (see the boundary between regimes II and III in Fig. 5), the Gouy-Chapman layer at the nanoparticle surface with the thickness l_{GC} becomes fully populated by counterions. The condensation parameter γ_0 reaches the crossover value $\gamma_{free}^*(\phi)$ at the corresponding volume fraction ϕ, calculated from eqn (23) using eqn (16) for the relation between r_{cm} and volume fraction ϕ:

$$\gamma_{free}^*(\phi) \approx \ln\left(\gamma_{free}^*\right) - \ln(\phi) \approx -\ln(\phi) \quad \text{spherical NPs} \qquad (24)$$

The last approximation in eqn (24) was obtained by ignoring the term $\ln(\gamma_{free}^*)$ since $\ln(\gamma_{free}^*) \ll \gamma_{free}^*$ for $\gamma_{free}^* \gg 1$. Upon further increase of the bare charge valence Z_0 and the corresponding increase of condensation parameter γ_0 at a constant volume fraction ϕ of NPs one enters the strong counterion condensation regime III with the normalized free charge valence saturating at $\gamma_{free}^*(\phi)$. The “free line” is the boundary between weak and strong condensation regimes (II and III) for a given condensation parameter γ_0 (red line in Fig. 5). This boundary is at the volume fraction of nanoparticles $\phi_{free}(\gamma_0)$ obtained from the expression in eqn (24):

$$\phi_{free}(\gamma_0) \approx \gamma_0 \exp(-\gamma_0) \quad \text{spherical NPs} \qquad (25)$$

The fraction of condensed counterions (eqn (23)) in solutions of spherical nanoparticles in the weak condensation regime II is given by the exponential value of the relative horizontal distance between the point $(\ln\phi, \gamma_0)$ in the diagram presented in Fig. 5 (point A) and the corresponding point $(\ln\phi_{free}, \gamma_0)$ on the “free” line – the boundary between regimes II and III at the same condensation parameter γ_0 in Fig. 5 (point B).

$$\frac{Z_{cond}}{Z_0} \approx \frac{\phi}{\phi_{free}(\gamma_0)} \approx \frac{\phi}{\gamma_0}\exp(\gamma_0) \quad \text{spherical NPs, regime II} \qquad (26)$$

Regime III: Strong counterion condensation regime ($\gamma_0 > \gamma_{free}^*(\phi)$). The strong electrostatic attraction to the particle forces the majority of counterions to condense near the particle surface ($x < l_c$, where l_c is the thickness of the condensed counterion zone) in the first minimum of the effective single counterion mean-field free energy $\Delta F_{eff}(x, r_{cm})$(red line in Fig. 4). A small fraction of counterions are free exploring the second free energy local minimum of $\Delta F_{eff}(x, r_{cm})$ at r_{cm} formed due to the lower entropic part of free energy there. The condensed counterions compensate the bare charge in a self-similar way. The counterion profile close to the surface (within this condensed counterion zone $x < l_c$) follows the Gouy-Chapman solution (eqns (11) and (12)). The effective valence at distances from the surface larger than the Gouy-Chapman length (for $x = r - r_0 > l_{GC}$) is almost independent of the bare valence of the nanoparticle. The effective surface charge number density $\sigma(r)$

in the condensed counterion zone near the nanoparticle surface in regime III is described by the Gouy-Chapman salt-free theory (eqn (11)):

$$\sigma(r_0+x)=\frac{\sigma_0}{1+x/l_{GC}}\approx\begin{cases}\sigma_0 & \text{for } x<l_{GC}\\ \dfrac{1}{l_B x} & \text{for } l_{GC}<x<l_c\end{cases} \qquad (27)$$

spherical NPs, regime III

The effective surface charge number density $\sigma(r)$ is almost constant and equal to the bare charge number density σ_0 at distance from the surface smaller than Gouy-Chapman length (for $x=r-r_0<l_{GC}$), but becomes independent of bare nanoparticle charge at distances from the surface larger than the Gouy-Chapman length (for $l_{GC}<x=r-r_0<l_c$) and decreases reciprocally with x (eqn (27)). The counterion concentration follows the self-similar profile at these length scales (eqn (12)):

$$c(r_0+x)\approx\frac{\gamma^2(r_0+x)}{r_0^2 l_B}\approx\begin{cases}\sigma_0^2 l_B & \text{for } x<l_{GC}\\ \dfrac{1}{l_B x^2} & \text{for } l_{GC}<x<l_c\end{cases} \qquad (28)$$

spherical NPs, regime III

The essence of the strong counterion condensation is that it reduces the effective charge number density from the bare value σ_0 to the “universal” effective value on the order of $(l_B x)^{-1}$ in the condensed counterion zone independent of the bare charge (see the red line with slope -1 for $l_{GC}<x<l_c$ in Fig. 6(a)). At distances from the nanoparticle surface larger than the thickness of the condensed counterion zone l_c, the counterion concentration dependence changes from inversely proportional to the square of the distance (see the red line with slope -2 for $l_{GC}<x<l_c$ in Fig. 6(b)) to exponentially decreasing with reciprocal distance from the spherical nanoparticle $\sim\exp(-Z_{free}/r)$ (see the red line for $l_c<x<r_{kT}$ in Fig. 6(b)) The effective charge valence is almost constant $Z(r)\approx Z_{free}$ (see the horizontal part of red line for $x>l_c$ in Fig. 6(a)), as there are not enough counterions in this empty zone to further reduce the effective charge. Most of the counterions outside the condensed counterion zone are free and located at $x>r_{kT}$. The bare condensation parameter γ_0 is reduced to the effective condensation parameter corresponding to the charge of free counterions $\gamma_{free}\equiv Z_{free}l_B/(2r_0)$ at the outer boundary $r=r_0+l_c$ of the condensed counterion zone with $\gamma_{free}=2\pi r_0 l_B\sigma(r_0+l_c)$ (eqn (15)). This effective condensation parameter γ_{free} of the nanoparticles in regime III at volume fraction ϕ (point C in Fig. 5) is almost the same as γ^*_{free} (eqn (24)) at the boundary between weak and strong counterion condensation regimes at the same volume fraction ϕ (point B in Fig. 5), which is independent of the bare nanoparticle charge valence $\gamma_0>\gamma^*_{free}$, and dependent only on volume fraction ϕ within regime III. The reason for this saturation of γ_{free} at γ^*_{free} is that the electrochemical potential in the condensed counterion zone does not change with the bare charge valence Z_0 due to the strong counterion condensation but only changes upon variation of volume fraction ϕ. The fraction of free counterions can be expressed by the relative vertical distance between point C in the diagram Fig. 5 $(\ln\phi,\gamma_0)$ and the corresponding point B at the same volume fraction ϕ of NPs on the “free” line (eqn (24)) – the boundary between strong and weak counterion condensation regimes (II and III) in Fig. 5 $(\ln\phi,\gamma^*_{free}(\phi))$.

$$\frac{Z_{free}}{Z_0}\approx\frac{\gamma^*_{free}(\phi)}{\gamma_0}\approx-\frac{\ln(\phi)}{\gamma_0} \quad \text{spherical NPs, regime III} \qquad (29)$$

3. Solutions of charged cylindrical nanoparticles

In this section, we describe the counterion distributions around cylindrical nanoparticles. We consider cylindrical nanoparticles with bare charge valence Z_0, radius r_0 and length L with $L\gg r_0$ (see Fig. 7). The bare surface charge number densities for cylindrical particles are (ignoring the upper and lower circular faces of the cylindrical particles):

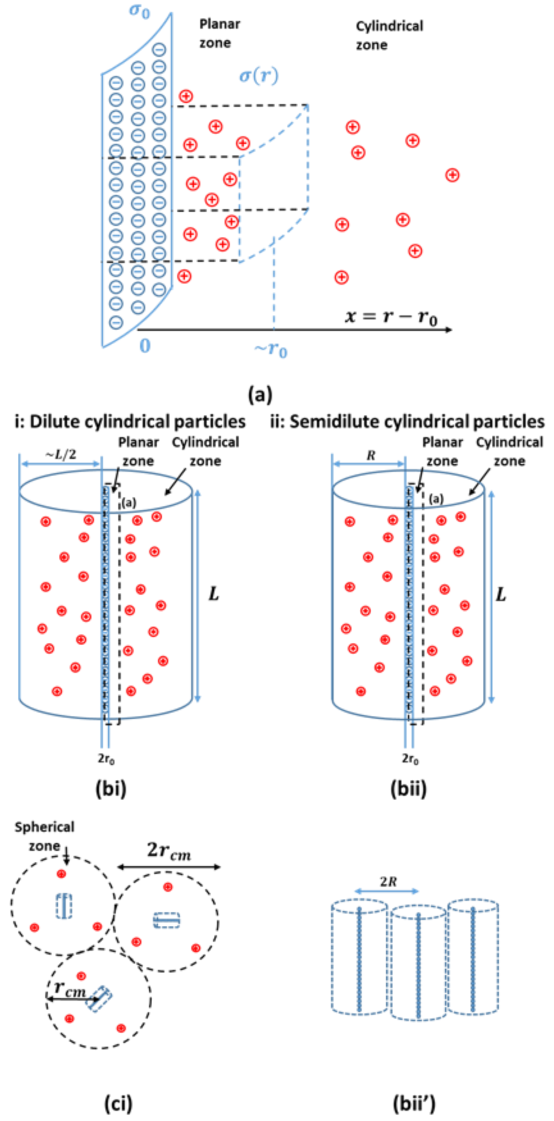

Fig. 7 (i) Dilute and (ii) semidilute solutions of negatively charged cylindrical nanorods. The symmetry of the electric field and the counterion distribution can be approximately divided into up to three zones: (a) planar symmetry zone for $x=r-r_0<r_0$; cylindrical symmetry zone of (bi) dilute cylindrical particles for $2r_0<r<L/2$ and (bii) semidilute cylindrical particles for $2r_0<r<R$ as the cylindrical zones pervade the solution shown in (bii'); (ci) spherical symmetry zone of dilute cylindrical particles for $L/2<r<r_{cm}$.

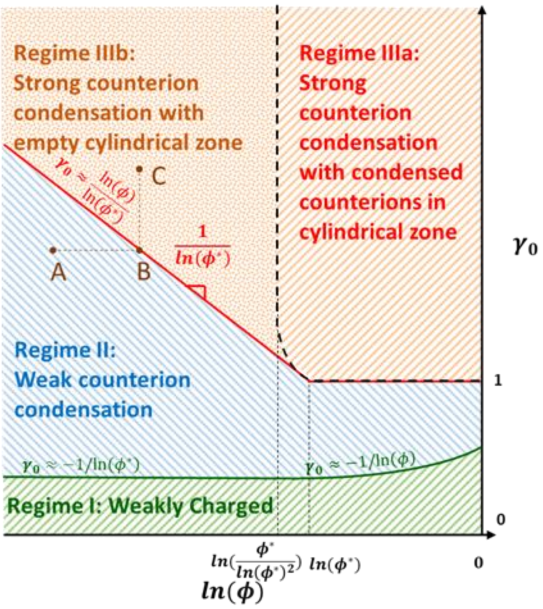

Fig. 8 Schematic diagram of the counterion regimes for charged cylindrical particles. Regime I: weakly charged particles (no counterion condensation); regime II: weak counterion condensation; regime III: strong counterion condensation. In regime III, there are two subregimes: subregime IIIa: strong counterion condensation with condensed counterions in cylindrical zone and regime IIIb: strong counterion condensation with empty cylindrical zone. Condensation parameter $\gamma_0 = Z_0 l_B / L$ is the nanoparticle valence normalized by the number of Bjerrum lengths l_B per nanoparticle size (see eqn (31)) and $\phi^* \approx (r_0/L)^2$ is the overlap concentration with the distances between the neighboring particles on the order of the cylindrical particle length L.

$$\sigma_0 = \frac{Z_0}{2\pi r_0 L} \quad \text{cylindrical NPs} \tag{30}$$

The bare normalized charge line number density γ_0 (the condensation parameter) for the cylindrical particles is:

$$\gamma_0 = \frac{Z_0 l_B}{L} = 2\pi\sigma_0 r_0 l_B \quad \text{cylindrical NPs} \tag{31}$$

Note that the condensation parameters γ_0 for both spherical (eqn (15)) and cylindrical (eqn (31)) nanoparticles are the number of elementary charges per area $2\pi r_0 l_B$. Similar to the spherical particles, the volume fraction is the product of physical volume and number density of nanoparticles. The physical volume of a cylindrical nanoparticle is $\sim r_0^2 L$ and the expression for the number density of cylindrical particles depends on whether the solution is dilute or semidilute, which is controlled by the relative magnitude of particle length L and average separation r_{cm} between the centers of neighboring nanoparticles. The solution is dilute if the particles on average are further apart from each other than their length $r_{cm} > L$ with number density $\sim r_{cm}^{-3}$ as for spherical particles (Fig. 7(ci)). The major qualitative difference between solutions of spherical and cylindrical particles is the existence of the semidilute solution regime with the average distance between the centers of neighboring nanorods less than their length $r_{cm} < L$ (Fig. 7(bii')). For semidilute solutions, the center-of-mass distance r_{cm} between two neighboring cylindrical particles is larger than the average closest distance between them (Fig. 7(bii')), called the correlation length[23] and denoted by 2R in this paper. This correlation length 2R is equivalent to the cell diameter in the cylindrical cell model[24,7,25] and the number density of cylindrical particles in semidilute solutions is proportional to $\sim(R^2L)^{-1}$. The volume fractions of cylindrical particles in dilute and semidilute regimes are: are further apart from each other than their length $r_{cm} > L$ with number density $\sim r_{cm}^{-3}$ as for spherical particles (Fig. 7(ci)).

$$\phi \approx \begin{cases} \dfrac{L r_0^2}{r_{cm}^3} & \text{dilute: } \phi < \phi^* = \dfrac{r_0^2}{L^2} \\ \dfrac{r_0^2}{R^2} & \text{semidilute: } \phi > \phi^* = \dfrac{r_0^2}{L^2} \end{cases} \quad \text{cylindrical NPs} \tag{32}$$

where the overlap volume fraction ϕ^* is the crossover between dilute and semidilute regimes. Similar to the spherical nanoparticles, the electric field can be approximated by planar symmetry very close to the smooth nanoparticle surface ($r - r_0 < r_0$, see Fig. 7(a)) and approximated by spherical symmetry in dilute solutions at distances larger than the nanoparticle size ($r - r_0 > L$, see Fig. 7(ci)). Besides the semidilute concentration regime (second line in eqn (32)), the difference between the spherical and cylindrical nanoparticles is the existence of the cylindrical symmetry zone (Fig. 7(b)) on length scales $r_0 < x = r - r_0 < L$ for dilute and $r_0 < x = r - r_0 < R$ for semidilute concentration regimes. The electric field in cylindrical zone is

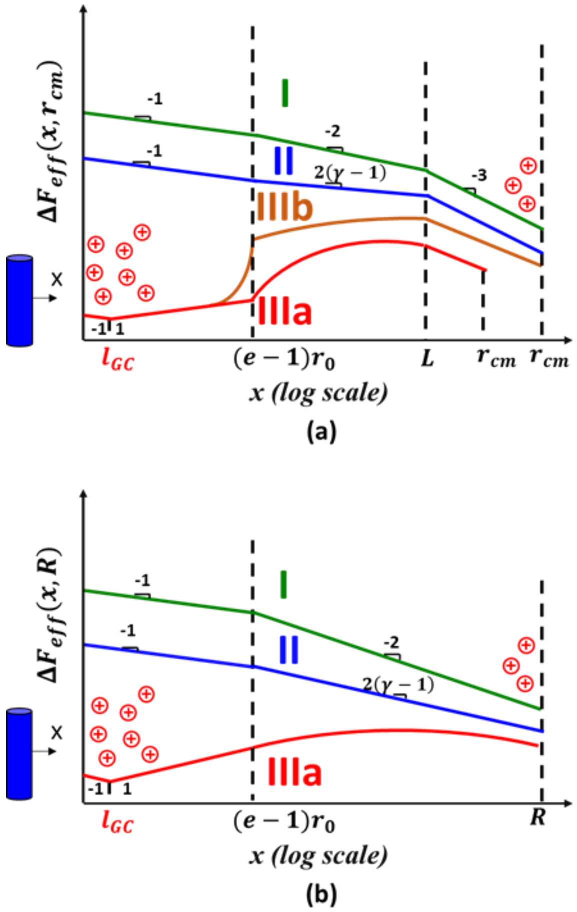

Fig. 9 Scaling dependence of the effective single counterion mean-field free energy (eqn (7)) on the distance $x = r - r_0$ from the surface of the charged cylindrical particles in (a) dilute and (b) semidilute solutions for three regimes: (I) weakly charged particles (green), (II) weak counterion condensation (blue), (III) strong counterion condensation: subregime IIIa with condensed counterions in cylindrical zone (red) and subregime IIIb with empty cylindrical zone (brown).

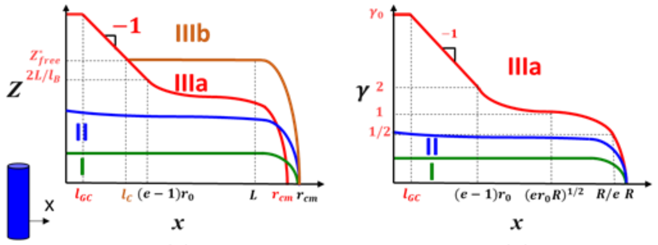

(a) (b)

Fig. 10 (a) Effective charge valence $Z(x)$ of dilute cylindrical particles and (b) effective charge line density $\gamma(x)$ of semidilute cylindrical particles as functions of the distance from the nanorod surface $x = r - r_0$. Weakly charged particles regime I (green), weak counterion condensation regime II (blue), strong counterion condensation subregime IIIa (red), and subregime IIIb (brown). All axes are logarithmic.

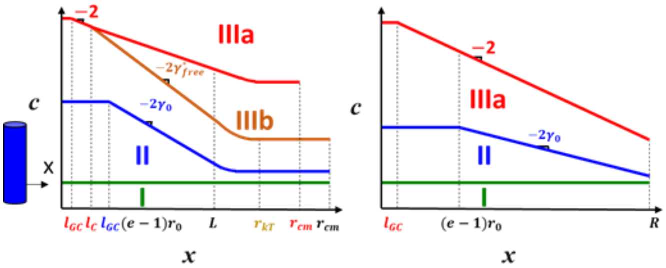

(a) (b)

Fig. 11 Counterion concentration $c(x)$ in (a) dilute and (b) semidilute charged cylindrical particle solution as functions of the distance from the nanorod surface $x = r - r_0$. Weakly charged particles regime I (green), weak counterion condensation subregime II (blue), strong counterion condensation subregime IIIa (red), and subregime IIIb (brown). All axes are logarithmic.

$$\left|\vec{E}(r)\right| \approx \frac{e\gamma(r)}{\varepsilon r},\ \gamma(r) = \gamma_0 - 2\pi\int_{r_0}^{r} c(r')r'dr' \qquad (33)$$
$$\text{cylindrical symmetry zone: } r < L$$

where $\gamma(r)$ is the normalized effective line charge density (see eqn (31) for $\gamma_0 \equiv \gamma(r_0)$). Similar to the spherical charged particles, there are three different counterion condensation regimes for cylindrical particles characterized by the condensation parameter γ_0 (eqn (31)) and the volume fraction ϕ (eqn (32)) – see Fig. 8: regime I of weakly charged particles ($\gamma_0 < -1/\ln(\phi^*)$ for dilute cylindrical particles and $\gamma_0 < -1/\ln(\phi)$ for semidilute cylindrical particles), regime II of weak counterion condensation ($-1/\ln(\phi^*) < \gamma_0 < \ln(\phi)/\ln(\phi^*)$ for dilute cylindrical particles and $-1/\ln(\phi) < \gamma_0 < 1$ for semidilute cylindrical particles), and regime III of strong counterion condensation ($\gamma_0 > \ln(\phi)/\ln(\phi^*)$ for dilute cylindrical particles and $\gamma_0 > 1$ for semidilute cylindrical particles). Note that there are two subregimes of regime III depending on whether there are condensed counterions located in the cylindrical zone (subregime IIIa in Fig. 8) or the cylindrical zone is empty (subregime IIIb in Fig. 8). For strong counterion condensation in semidilute solutions, there are always condensed counterions in cylindrical zone corresponding to subregime IIIa. At the crossover between subregimes IIIa and IIIb in dilute nanorod solutions (vertical dashed line in Fig. 8), there is one counterion per Bjerrum length condensed in the cylindrical zone (see red and brown lines in Fig. 10(a)). Typical parameters for each regime are listed in Appendix A.

Below we discuss the counterion distribution of the corresponding regimes of charged cylindrical particles (Fig. 8).

Regime I. Weakly charged particles:
$\gamma_0 < -1/\ln(\phi^*)$ for dilute cylindrical particles and $\gamma_0 < -1/\ln(\phi)$ for semidilute cylindrical particles.

Similar to the spherical particle regime I, the majority of counterions are far away from the weakly charged nanoparticle surface and are almost uniformly distributed throughout the whole solution. The effective charge valence does not vary significantly with distance r from the nanocylinders $Z(r) \approx Z_0$ up to length scales on the order of separation between particles ($r \sim r_{cm}$ for dilute cylindrical particles or $r \sim R$ for semidilute cylindrical particles) indicated by the horizontal part of the green lines in Fig. 10. The electrostatic potential can be approximated by the potential due to the bare charge valence Z_0 which is almost uncompensated up to length scales on the order of separation between particles. The electrostatic potential in the cylindrical zone varies logarithmically with the distance from the nanocylinder axis (eqn (1b)):

$$e\Delta\psi(r,r') \approx 2kT\gamma_0 \ln(r/r') \qquad (34)$$
$$\text{uncompensated cylindrical zone}$$

The condition for the counterion electrostatic energy difference between particle surface and average distance between particles to be smaller than kT is for dilute cylindrical particles: $|e\Delta\psi(r_0, r_{cm})| \approx |e\Delta\psi(r_0, L)| \approx 2\gamma_0 kT\ln(L/r_0) \approx -\gamma_0 kT\ln(\phi^*) < kT$ and for semidilute cylindrical particles $|e\Delta\psi(r_0, R)| \approx 2\gamma_0 kT\ln(R/r_0) \approx -\gamma_0 kT\ln(\phi) < kT$ (eqn (32)). Thus the entire solution is the free zone with the variation of counterion concentration by less than a factor of e (see horizontal green lines in Fig. 11) and there is no counterion condensation in regime I.

Regime II. Weak counterion condensation:
$-1/\ln(\phi^*) < \gamma_0 < \ln(\phi)/\ln(\phi^*)$ for dilute nanocylinders and $-1/\ln(\phi) < \gamma_0 < 1$ for semidilute nanocylinders.

In this regime, the variation of the counterion electrostatic energy is larger than kT (for dilute cylindrical particles: $|e\Delta\psi(r_0, r_{cm})| > |e\Delta\psi(r_0, L)| > kT$ and for semidilute cylindrical particles $|e\Delta\psi(r_0, R)| > kT$) and less than half of all counterions are condensed in the weak counterion condensation regime. Due to the low volume fraction ϕ, the majority of counterions are still far away from the particle surface attracted by the free energy minimum of $\Delta F_{eff}(x, r_{cm})$ at $x \approx r_{cm}$ or R dominated by counterion entropy (see the blue lines in Fig. 9). The counterion concentration profile in the cylindrical zone is a power law with exponent $-2\gamma_0$, as expected from the Boltzmann factor (eqns (20) and (34)) of the logarithmically varying electrostatic potential:

$$c(r) \sim \exp\left(-\frac{e\Delta\psi}{kT}\right) \sim r^{-2\gamma_0} \qquad (35)$$
$$\text{uncompensated cylindrical zone}$$

The counterion distribution in the cylindrical zone is determined by the integral of the counterion concentration:

$$\int c(r)rdr \sim \int r^{1-2\gamma_0}dr \sim r^{2(1-\gamma_0)}\Big|_{r_0}^{L \text{ or } R} \qquad (36)$$

The integral is either dominated by the lower limit of the integral (at r_0) or by the upper limit of the integral (at L for dilute nanocylinders or R for semidilute cylinders) depending on whether γ_0 is bigger or smaller than 1 (eqn (36)). In the entire semidilute weak counterion condensation regime II and the lower part of dilute weak counterion condensation regime II of nanocylinders with $\gamma_0 < 1$, the integral of the counterion concentration (eqn (36)) is dominated by the upper limit. The majority of condensed counterions are located in the cylindrical zone on the length scale of l_c from the charged nanocylinder. In this regime, there is no empty zone and the outer boundary of condensed counterion zone l_c coincides with the inner boundary of free zone r_{kT}:

$$l_c \approx r_{kT} \approx \begin{cases} L\exp\left(-\dfrac{1}{2\gamma_0}\right) & \text{dilute cylindrical NPs,} \\ R\exp\left(-\dfrac{1}{2\gamma_0}\right) & \text{semidilute cylindrical NPs} \end{cases} \quad (37)$$
$$\gamma_0 < 1 \text{ in regime II}$$

The electrostatic energy of these weakly condensed counterions with respect to regions in the solution with zero field is on the order of, but larger than, thermal energy kT. For semidilute nanocylinders with very large aspect ratio $\ln(R/r_0) \gg 1$ in regime II with $1/\ln(\phi) < \gamma_0 < 1$, the asymptotic analytical solution[24,7,25] for the fraction of condensed counterions Z_{cond}/Z_0 is found to be half of the condensation parameter γ_0:

$$\frac{Z_{cond}}{Z_0} \approx \frac{\gamma_0}{2} \quad \text{semidilute cylindrical NPs, regime II} \quad (38)$$

In the upper part of dilute weak counterion condensation regime II of nanocylinders with $\gamma_0 > 1$, the integral of counterion concentration (eqn (36)) is dominated by the lower limit at r_0. In this case, the Gouy-Chapman length is smaller than the radius of the cylindrical charged particles $l_{GC} \approx r_0/\gamma_0 < r_0$. The majority of condensed counterions are within the Gouy-Chapman length in the planar zone $x < l_{GC}$. The number of condensed counterions in this case can be estimated by the counterion concentration at the nanoparticle surface $c(r_0) \sim Z_0/r_{cm}^3 \exp(-e\Delta\psi(r_0, r_{cm})/kT)$ (eqn (20)) times the volume of a layer with the thickness of Gouy-Chapman length $l_{GC} \sim r_0/\gamma_0$ (eqn (4)) around the nanocylinders.

$$Z_{cond} \approx c(r_0) l_{GC} r_0 L \approx \frac{L}{l_B} \frac{\phi}{(\phi^*)^{\gamma_0}} \exp(\gamma_0) \quad (39)$$
$$\text{regime II, dilute cylindrical NPs}$$

Compared to the similar regime II for spherical NPs with the same condensation parameter $\gamma_0 > 1$ (eqn (23)), the number of condensed counterions for cylindrical NPs is larger by the factor $(\phi^*)^{-\gamma_0}$. This extra factor is due to the logarithmic variation of electrostatic potential in the cylindrical zone $|e\Delta\psi(r_0, L)| \approx 2\gamma_0 kT \ln(L/r_0) \approx -\gamma_0 kT \ln(\phi^*)$. This extra factor leads to a higher counterion concentration at the surface $c(r_0)$ of cylindrical particles with a large aspect ratio $L \gg r_0$. At the upper boundary of the weak counterion condensation regime, the concentration of condensed counterions at the nanoparticle surface $c(r_0)$ reaches the Gouy-Chapman concentration $c_{GC} \approx \gamma_0^2/(l_B r_0^2)$ (eqns (10) and (31)). At this crossover between weak and strong condensation regimes for dilute cylindrical particles with $\gamma_0 > 1$ (see point B at the boundary between regimes II and III in Fig. 8), the Gouy-Chapman layer at the nanoparticle surface with the thickness l_{GC} becomes fully populated by counterions. The condensation parameter γ_0 reaches the crossover value $\gamma^*_{free}(\phi)$ at the corresponding volume fraction ϕ (red line in Fig. 8), calculated from eqn (39) using eqns (31) and (32) for the relation between r_{cm} and volume fraction ϕ:

$$\gamma^*_{free}(\phi) \approx \frac{\ln(\gamma^*_{free}) - \ln(\phi)}{-\ln(\phi^*)} \approx \frac{\ln(\phi)}{\ln(\phi^*)} \quad (40)$$
$$\text{dilute cylindrical NPs}$$

Upon increase of the bare charge valence Z_0 and the corresponding increase of condensation parameter γ_0 at a constant volume fraction ϕ of NPs in the strong counterion condensation regime III, the normalized free charge valence saturates at $\gamma^*_{free}(\phi)$. The corresponding volume fraction $\phi_{free}(\gamma_0)$ at the boundary between regime II and III is estimated from eqn (40):

$$\phi_{free}(\gamma_0) \approx \gamma_0 (\phi^*)^{\gamma_0} \exp(-\gamma_0) \quad \text{dilute cylindrical NPs} \quad (41)$$

The fraction of condensed counterions (eqn (39)) in solutions of dilute cylindrical nanoparticles in the weak condensation regime II is given by the exponential value of the relative horizontal distance between the point $(\ln\phi, \gamma_0)$ in the diagram (point A in Fig. 8) and the corresponding point $(\ln\phi_{free}, \gamma_0)$ on the “free” line – the boundary between regimes II and III at the same condensation parameter γ_0 (point B in Fig. 8).

$$\frac{Z_{cond}}{Z_0} \approx \frac{\phi}{\phi_{free}(\gamma_0)} \approx \frac{\phi}{\gamma_0} (\phi^*)^{-\gamma_0} \exp(\gamma_0) \quad (42)$$
$$\text{cylindrical NPs in regime II}$$

Regime III. Strong counterion condensation: $\gamma_0 > \ln(\phi)/\ln(\phi^*)$ for dilute and $\gamma_0 > 1$ for semidilute cylindrical particles.

Similar to the strong counterion condensation regime III for solutions of spherical charges, more than half of counterions are condensed. However, the difference between counterion profiles of regime III for cylindrical and spherical particles is that a fraction of condensed counterions can be located in the cylindrical zone. There are two subregimes: subregime IIIa with condensed counterions in cylindrical zone and subregime IIIb with empty cylindrical zone. Below we separately discuss semidilute subregime IIIa, dilute subregime IIIa, and dilute subregime IIIb.

Subregime IIIa. semidilute cylindrical particles ($\gamma_0 > 1, \phi > \phi^*$)

In Regime I, the entire planar zone and cylindrical zone are free zones as there are no condensed counterions (see green line in Fig. 10(b)). In semidilute Regime II, the counterions start to condense. Both the fraction of the condensed counterions Z_{cond}/Z_0 (eqn (38)) and the outer boundary of condensed counterion zone l_c (eqn (37)) increase with γ_0. As the condensation parameter γ_0 increases from $\gamma_0 = -1/\ln(\phi)$ to $\gamma_0 = 1$ in semidilute Regime II, the condensed counterions fill in the outer part of the cylindrical zone further away from the surface of nanocylinders. At the boundary $\gamma_0 = 1$ between semidilute Regime II and Regime IIIa, ½ counterion per Bjerrum length is condensed in the outer part of cylindrical zone $(er_0R)^{1/2} < x < R/e$ (see blue line in Fig. 10 at $\gamma_0 = 1$) and the other ½ counterion per Bjerrum length is free between $\mathrm{R/e} < \mathrm{x} < \mathrm{R}$ (see green line in Fig. 12 at $\gamma_0 = 1$).

In Regime IIIa, the condensation parameter $\gamma_0 > 1$ and counterions start to fill the planar and the inner half of cylindrical zone $0 < \mathrm{x} = \mathrm{r} - \mathrm{r}_0 < (\mathrm{er}_0\mathrm{R})^{1/2}$, as the integral of counterion concentration (eqn (36)) becomes dominated by the lower limit $\mathrm{r} = \mathrm{r}_0$. The number of counterions in the outer half of cylindrical zone (on logarithmic scales) saturates with 1 counterion per Bjerrum length (½ condensed counterion at distance $(\mathrm{er}_0\mathrm{R})^{1/2} < \mathrm{x} < \mathrm{R/e}$ shown by blue line in Fig. 12 and ½ free counterion at distance $\mathrm{R/e} < \mathrm{x} < \mathrm{R}$ shown by green line in Fig. 12). For $1 < \gamma_0 < 2$, the remaining $\gamma_0 - 1$ counterions per Bjerrum length condense in the planar zone and the inner half of cylindrical zone $0 < \mathrm{x} < (\mathrm{er}_0\mathrm{R})^{1/2}$. About half of these $\gamma_0 - 1$ counterions are located in the planar zone $0 < \mathrm{x} < (\mathrm{e} - 1)\mathrm{r}_0$ and the other half of $\gamma_0 - 1$ counterions are distributed in the inner part of cylindrical zone $(\mathrm{e} - 1)\mathrm{r}_0 < \mathrm{x} < (\mathrm{er}_0\mathrm{R})^{1/2}$.

Above $\gamma_0 = 2$, the number of counterions in the inner half of the cylindrical zone ($(\mathrm{e} - 1)\mathrm{r}_0 < \mathrm{x} < (\mathrm{er}_0\mathrm{R})^{1/2}$) further increases and saturates at 1 for $\gamma_0 \gg 1$ (red line in Fig. 12) while the other $\gamma_0 - 2$ counterions are distributed in the planar zone. The equal number of counterions (one counterion per Bjerrum length) for $\gamma_0 \gg 1$ distributed close to the inner ($\mathrm{r} = \mathrm{er}_0$) and close to the outer ($\mathrm{r} = \mathrm{R}$) boundaries of the cylindrical zone can be approximated by the zero free-energy difference between these regions $\Delta\mathrm{F}_{\mathrm{eff}}(\mathrm{er}_0, \mathrm{R}) = 0$ (red line in Fig. 9(b)) and described by

$$\Delta F_{eff}\left(er_0,R\right) \approx -2kT\ln\left(er_0/R\right) + e\Delta\psi\left(er_0,R\right)$$
$$\approx -kT\ln\left(\frac{e^2r_0^2c\left(er_0\right)}{R^2c\left(R\right)}\right) \approx 0 \qquad (43)$$
$$\text{semidilute cylindrical NPs, regime III}$$

(see eqn (7) and (63)) with asymptotic dependence of $2\pi\mathrm{r}^2\mathrm{l}_\mathrm{B}\mathrm{c}(\mathrm{x})$ for $\gamma_0 \gg 1$ presented by the dashed line in Fig. 13. The minimum of $\mathrm{r}^2\mathrm{c}(\mathrm{r})$ (see Fig. 13) corresponds to the free energy maximum at $\mathrm{r} = (\mathrm{eRr}_0)^{1/2}$ with $\Delta\mathrm{F}_{\mathrm{eff}}\left((\mathrm{eRr}_0)^{1/2}, \mathrm{R}\right) \approx 2\mathrm{kTln}[\ln(\mathrm{eR/r}_0)/\pi]$ (red line in Fig. 9(b)).

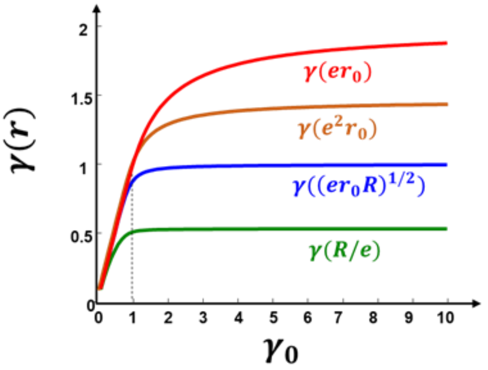

Fig. 12 The effective line charge densities $\gamma(\mathrm{r})$ for semidilute cylindrical particles at four different distances $\mathrm{r} = \mathrm{er}_0$ (red line), $\mathrm{r} = \mathrm{e}^2\mathrm{r}_0$ (brown line), $\mathrm{r} = (\mathrm{er}_0\mathrm{L})^{1/2}$ (blue line), and $\mathrm{r} = \mathrm{R/e}$ (green line) from the nanocylinder axis as functions of condensation parameter γ_0. At $\gamma_0 = 1$, the effective line charge density $\gamma(\mathrm{R/e})$ (green curve) saturates at 0.5 and the effective line charge density $\gamma((\mathrm{er}_0\mathrm{R})^{1/2})$ (blue curve) converges to 1. At $\gamma_0 \gg 1$, the effective line charge density at the inner boundary of the cylindrical zone $\gamma(\mathrm{er}_0)$ (red curve) approaches 2 and $\gamma(\mathrm{e}^2\mathrm{r}_0)$ (brown curve) approaches 1.5.

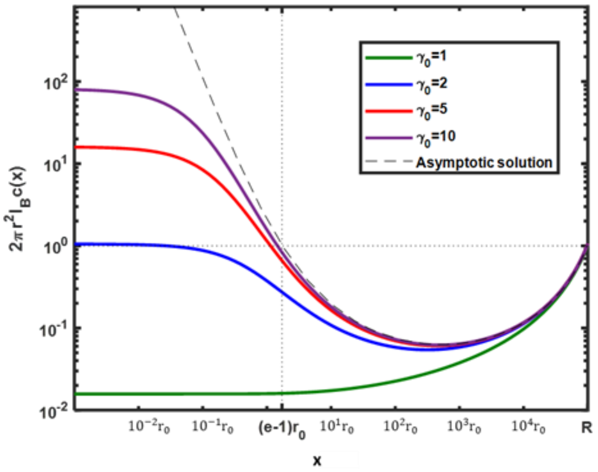

Fig. 13 Numerical solution of normalized counterion concentration profile for different values of bare linear charge density (green: $\gamma_0 = 1$, blue: $\gamma_0 = 2$, red: $\gamma_0 = 5$, and purple: $\gamma_0 = 10$ with $\mathrm{R} = 10^5\mathrm{r}_0$ and $\gamma_\mathrm{R} = 0$). The solution gradually converges to the asymptotic solution (dashed line) with increasing condensation parameter γ_0. The deviation of $2\pi\mathrm{r}^2\mathrm{l}_\mathrm{B}\mathrm{c}(\mathrm{r})$ for the dashed line from 1 is described by eqn (63).

The spatial distribution of $\gamma_0 - 2$ counterions in planar zone is well described by the Gouy-Chapman solution. The counterion profile converges towards the asymptotic analytical solution presented in Appendix C with effective line charge density (see also eqn (61)):

$$\gamma\left(r\right) \approx \begin{cases} 1+\dfrac{r_0}{x} & l_B < l_{GC} < x = r - r_0 \ll r_0 \quad (a) \\ 1+\dfrac{1}{\ln\left(r/r_0\right)} & er_0 \le r \ll \left(er_0R\right)^{1/2} \quad (b) \\ \dfrac{\ln\left(R/r\right)}{\ln\left(R/r\right)+1} & \left(er_0R\right)^{1/2} \ll r < R \quad (c) \end{cases} \qquad (44)$$
$$\text{semdilute cylindrical NPs, regime III for } \gamma_0 >> 1$$

and counterion concentration distribution function (see eqn (60)):

$$c\left(r\right) \approx \begin{cases} \dfrac{1}{2\pi x^2 l_B} & l_B < l_{GC} < x = r - r_0 \ll r_0 \quad (a) \\ \dfrac{1}{2\pi r^2 l_B}\dfrac{1}{\left[\ln\left(r/r_0\right)\right]^2} & er_0 \le r \ll \left(er_0R\right)^{1/2} \quad (b) \\ \dfrac{1}{2\pi r^2 l_B}\dfrac{1}{\left[\ln\left(r/eR\right)\right]^2} & \left(er_0R\right)^{1/2} \ll r < R \quad (c) \end{cases} \qquad (45)$$
$$\text{semidilute cylindrical NPs, regime III for } \gamma_0 >> 1$$

The approximations at different length scales in eqns (44) and (45) are obtained by the Taylor expansion of trigonometric and logarithmic functions. The analytical solutions in the planar zone (eqns (44a) and (45a)) are similar to the Gouy-Chapman solution (eqns (11) and (12)). Note that with the mean-field approximation discussed in the introduction, eqns (44) and (45) only work for $\sigma_0 < 2\pi\mathrm{l}_\mathrm{B}^{-2}$ or $\gamma_0 < \mathrm{r}_0/\mathrm{l}_\mathrm{B}$ (eqn (31)), which determines the lower boundary of eqns (44a) and (45a).

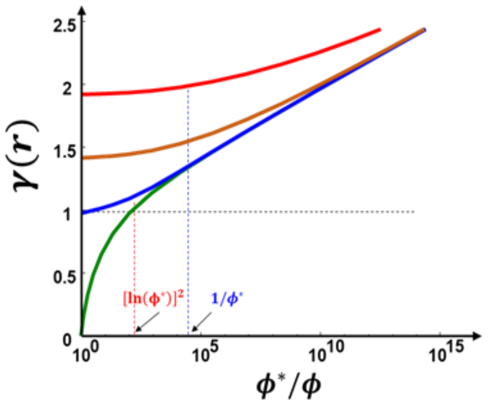

Fig. 14 The effective line charge density $\gamma(\mathrm{r})$) for dilute cylindrical particles with $\gamma_0 = 10$ and $\phi^* = 10^{-10}$ at four different distances $\mathrm{r} = \mathrm{er}_0$ (red line), $\mathrm{r} = \mathrm{e}^2\mathrm{r}_0$ (brown line), $\mathrm{r} = (\mathrm{er}_0\mathrm{L})^{1/2}$ (blue line), and $\mathrm{r} = \mathrm{L}$ (green line) from the nanocylinder axis. Upon dilution, the counterions from the outer part of cylindrical zone escape to the spherical zone – see the sharp increase of the left part of the green line as it approaches the blue line. At $\phi \approx \phi^*/[\ln(\phi^*)]^2$ (red vertical dotted line), the outer cylindrical zone becomes almost empty as the effective line charge density $\gamma(\mathrm{L})$ (green curve) approaches the value of $\gamma((\mathrm{er}_0\mathrm{L})^{1/2})$ (blue curve). At $\phi \approx \phi^{*2}$ (blue vertical dotted line), the counterions starts to escape from the planar zone as the effective line charge density at the inner boundary of the cylindrical zone $\gamma(\mathrm{er}_0)$ (red curve) becomes larger than 2 and the fraction of counterions in the inner cylindrical zone also decrease as $\gamma((\mathrm{er}_0\mathrm{L})^{1/2})$ (blue curve) approaches the values of $\gamma(\mathrm{er}_0)$ (red curve) and $\gamma(\mathrm{e}^2\mathrm{r}_0)$ (brown curve).

Subregime IIIa. dilute cylindrical particles with counterions condensed in cylindrical zone ($\phi^*/[\ln(\phi^*)]^2 < \phi < \phi^*$)

Upon dilution of cylindrical particles (increasing $\mathrm{r}_{\mathrm{cm}}/\mathrm{L}$), the counterions start to escape into the spherical zone as the effective single counterion free energy difference across the spherical zone increases, $\Delta\mathrm{F}_{\mathrm{eff}}(\mathrm{L},\mathrm{r}_{\mathrm{cm}}) \sim 3\mathrm{kTln}(\mathrm{r}_{\mathrm{cm}}/\mathrm{L})$ (see red line in Fig. 9(a)). The counterions initially escape from the outer part of cylindrical zone (see Fig. 14). Recall that with the increasing γ_0 at higher volume fractions this outer part of cylindrical zone gets filled with counterions first before counterions condense into inner sections of cylindrical zone. The magnitude of electrostatic energy of counterions in the outer part of cylindrical zone is the lowest as the strength of their electrostatic attraction to the charged nanocylinder is the weakest. This is the reason the counterions located there are the first to escape into spherical zone with decreasing volume fraction ϕ and increasing entropy of free counterions in spherical zone. The outer part of cylindrical zone ($(\mathrm{er}_0\mathrm{L})^{1/2} < \mathrm{x} < \mathrm{L}$) becomes empty when the one counterion per Bjerrum length escapes to the spherical zone and the effective line charge density at the outer boundaries of the cylindrical zone approaches unity $\gamma\left((\mathrm{er}_0\mathrm{L})^{1/2}\right) \approx \gamma(\mathrm{L}) \approx 1$ with $\mathrm{l}_\mathrm{c} = (\mathrm{eLr}_0)^{1/2}$ (see Fig. 14). The escape of one counterion per Bjerrum length determines the regime boundary between subregimes IIIa and IIIb as it corresponds to half of the counterions of the cylindrical zone leaving it for spherical zone. It is also the phase boundary of the analytical solutions between the saturated condensation and the unsaturated condensation[7]. The particle volume fraction corresponding to one counterion per Bjerrum length escaping from the cylindrical zone and becoming free in spherical zone can be estimated by balancing the effective free energies at the outer boundary of spherical zone, r_{cm}, and the inner boundary of cylindrical zone $\Delta\mathrm{F}_{\mathrm{eff}}(\mathrm{er}_0,\mathrm{r}_{\mathrm{cm}}) \approx 2\mathrm{kTln}[\ln(\mathrm{eL}/\mathrm{r}_0)] - 3\mathrm{kTln}(\mathrm{r}_{\mathrm{cm}}/\mathrm{L}) \approx 0$ estimated from eqns (7) and (43) as the counterion free energy in the inner part of the cylindrical zone is not affected by the escaping counterions. This free energy balance gives the boundary $\phi(\gamma(\mathrm{L}) \approx 1\,) \approx \phi^*/[\ln(\phi^*)]^2$ separating subregimes IIIa and IIIb (see the vertical dashed line in Fig. 8 and red vertical dashed line in Fig. 14). For example, for nanorods with an aspect ratio of $\mathrm{L}/\mathrm{r}_0 = 100$, the volume fraction at the crossover between subregime IIIa and IIIb is $\phi(\gamma(\mathrm{L}) \approx 1\,) \approx \phi^*/85$ two decades below the overlap concentration $\phi^* \approx 10^{-4}$. At higher volume fractions $\phi > \phi^*/[\ln(\phi^*)]^2$ corresponding to subregime IIIa (to the right of dashed line in Fig. 8), there is more than one condensed counterion per Bjerrum length in the cylindrical zone corresponding to the saturated condensation in the Deshkovski cell model[7] with $\gamma(\mathrm{L}) \leq 1$. The counterion distribution in the inner part of cylindrical zone (see $\mathrm{er}_0 < \mathrm{r} < (\mathrm{eLr}_0)^{1/2}$ part of red line in Fig. 10(a)) in subregime IIIa is similar to that in semidilute solution (see $\mathrm{er}_0 < \mathrm{r} < (\mathrm{eLr}_0)^{1/2}$ part of red line in Fig. 10(b)). However, as more counterions escape from the cylindrical zone, the thickness of condensed counterion layer l_c decreases from L/e in semidilute regime IIIa, opening up the empty zone $\mathrm{l}_\mathrm{c} < \mathrm{x} < \mathrm{r}_{\mathrm{kT}}$ in the outer shell of the cylindrical zone ($(\mathrm{eLr}_0)^{1/2} < \mathrm{l}_\mathrm{c} < \mathrm{L}$). At the boundary between subregimes IIIa and IIIb for dilute cylindrical particles, the outer boundary of the condensed counterion zone is $\mathrm{l}_\mathrm{c} \approx (\mathrm{eLr}_0)^{1/2}$, while the inner boundary of the free counterion zone is $\mathrm{r}_{\mathrm{kT}} \approx \mathrm{L}$ and thus the empty zone is the outer part of cylindrical zone $(\mathrm{eLr}_0)^{1/2} < \mathrm{r} < \mathrm{L}$.

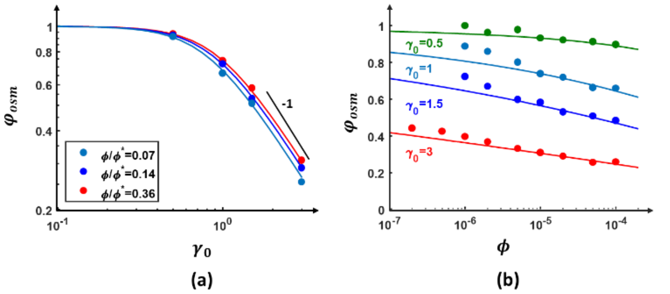

(a) (b)

Fig. 15 The osmotic coefficient φ_{osm} of dilute charged rod-like particles (a) as a function of condensation parameter $\gamma_0 = Z_0 l_B/L$ at volume fractions $\phi/\phi^* = 0.07, 0.14, 0.36$ with $\phi^* = 1.4 \times 10^{-4}$; (b) as a function of polymer volume fraction ϕ at condensation parameter γ_0=0.5, 1, 1.5 and 3. Filled circles are simulation data of Liao et al.[27] and solid lines are obtained from the crossover function eqn (51) between the osmotic coefficient of unity in regime I and eqn (50) in regime III for cylindrical particles, with the fitting parameters $c_1 = 0.72$ and $\mathrm{c}_2 = 2.56$.

Subregime IIIb. dilute cylindrical particles with empty cylindrical zone ($\phi < \phi^*/[\ln(\phi^*)]^2$)

At lower volume fractions $\phi < \phi^*/[\ln(\phi^*)]^2$ in the subregime IIIb (to the left of dashed line in Fig. 8), there is less than one counterion per Bjerrum length in the cylindrical zone ($\mathrm{er}_0 < \mathrm{r} < (\mathrm{er}_0\mathrm{L})^{1/2}$) and more than half of the cylindrical zone on the logarithmic scale is empty (see the horizontal part of the brown line in Fig. 10(a)). This empty zone with almost no counterions is located at distances between $\mathrm{l}_\mathrm{c} < \mathrm{x} < \mathrm{r}_{\mathrm{kT}}$ from nanorod surface with the outer boundary of the empty zone $\mathrm{r}_{\mathrm{kT}} \sim \gamma_{\mathrm{free}}\mathrm{L} > \mathrm{L}$ (eqn (46)) in the spherical zone and the inner boundary of the empty zone (outer boundary of the condensed counterion zone) l_c becoming smaller than $(er_0L)^{1/2}$.

At higher dilution, more counterions escape from the cylindrical zone and the cylindrical zone becomes almost completely empty when $\gamma(L) > 2$ at a volume fraction $\phi < \phi^{*2}$ calculated from the balance of the chemical potentials[26] (see blue vertical dashed line in Fig. 14). The thickness l_c of the condensed counterion layer becomes smaller than the radius r_0 of the cylindrical particles (see the brown line in Fig. 10(a)). This narrow condensed counterion layer is well-described by the Gouy-Chapman solution for the strong counterion condensation in the planar zone. Similar to the spherical particles, the normalized free charge valence is independent of bare charge valence in regime IIIb (point C in Fig. 8) and is determined by the value $\gamma^*_{free}(\phi)$ on the “free line” of the diagram (point B in Fig. 8) at the same nanoparticle volume fraction ϕ. The fraction of free counterions can then be expressed by the relative vertical distance between point C ($\ln\phi, \gamma_0$) on the diagram and the corresponding point B ($\ln\phi, \gamma^*_{free}(\phi)$) on the “free” line (eqn (40)) – the boundary between strong and weak counterion condensation regimes (II and IIIb) at the same volume fraction ϕ of NPs.

$$\frac{Z_{free}}{Z_0} \approx \frac{\gamma^*_{free}(\phi)}{\gamma_0} \approx \frac{\ln(\phi)}{\gamma_0 \ln(\phi^*)} \qquad (46)$$

dilute cylindrical NPs regime IIIb

4. Osmotic pressure in solutions of charged particles

The osmotic pressure of charged particles in the salt-free regime is dominated by the counterion contribution as there are many free counterions per charged particle. The osmotic pressure due to the counterions is determined by the counterion concentration at locations equidistant to neighboring particles, $c_{free} = c(r_{cm})$ for spherical and dilute cylindrical particles or $c_{free} = c(R)$ for semidilute cylindrical particles, where the electric field is almost zero due to the compensation of the nanoparticle charge by counterions. Therefore, osmotic pressure can be estimated as the pressure of an "ideal gas" of “free” counterions.

$$\Pi = kTc_{free} = \begin{cases} kTc(r_{cm}) & \text{spherical and dilute cylindrical NPs} \\ kTc(R) & \text{semidilute cylindrical NPs} \end{cases} \qquad (47)$$

The osmotic coefficient φ_{osm} is defined as the ratio of osmotic pressure Π to the ideal gas pressure of all counterions if they were all free. The osmotic coefficient is therefore equal to the fraction of free counterions by assuming that free counterions are uniformly distributed over the whole solution:

$$\varphi_{osm} \approx \frac{Z_{free}}{Z_0} \approx \begin{cases} \dfrac{c(r_{cm})r_{cm}^3}{Z_0} & \text{spherical and dilute cylindrical NPs} \\ \dfrac{c(R)R^2L}{Z_0} & \text{semidilute cylindrical NPs} \end{cases} \qquad (48)$$

For spherical and dilute cylindrical particles, the osmotic coefficient is almost unity in regime I ($\gamma_0 < 1$ for spherical particles and $\gamma_0 < -1/\ln(\phi^*)$ for dilute cylindrical particles) and on the order of unity (between ½ and 1) in regime II ($\gamma_0 < \gamma^*_{free}$, eqns (24) and (40)) with most of the counterions far away from the charged particles

$$\varphi_{osm} \sim 1,\ c_{free} \approx \frac{Z_0}{r_{cm}^3},\ \Pi \approx kT\frac{Z_0}{r_{cm}^3} \qquad (49)$$

spherical and dilute cylindrical NPs regimes I & II

In regime III ($\gamma_0 > 1$ with $\phi > \phi^*_{free}$, eqns (25) and (41)), the osmotic coefficient $Z_{free}/Z_0 = \gamma_{free}/\gamma_0$ is inversely proportional to the condensation parameter γ_0 due to the saturation of the effective charge valence at $\gamma_{free}(\phi)$ (see eqns (29) and (46)):

$$\varphi_{osm} \approx \begin{cases} -\dfrac{\ln(\phi)}{\gamma_0} & \text{spherical NPs regime III} \\ \dfrac{\ln(\phi)}{\gamma_0 \ln(\phi^*)} & \text{dilute cylindrical NPs regime IIIb} \end{cases} \qquad (50)$$

We compare the scaling prediction for the dependences of the osmotic coefficient φ_{osm} (eqn (50)) on the condensation parameter γ_0 (Fig. 15 (a)) and the volume fraction ϕ (Fig. 15(b)) with the results of the molecular dynamic simulation of Liao et al.[27] for dilute charged rod-like nanoparticles. The simulation data are fitted to the expression approximating the crossover between eqn (49) for regime I with $\varphi_{osm} \cong 1$ and eqn (50) for regime III with hyperbolic dependence on condensation parameter γ_0 and logarithmic dependence on volume fraction ϕ:

$$\varphi_{osm} = \left[1 + \left(\frac{c_1 \ln(\phi)}{\gamma_0 \ln(\phi^*)}\right)^{-c_2}\right]^{-1/c_2} \qquad (51)$$

The two adjustable parameters $c_1 = 0.72$ and $c_2 = 2.56$ allow simultaneous fit of data in both Fig. 15(a) and Fig. 15(b). The osmotic coefficient decreases from $\varphi_{osm} \cong 1$ in regime I to $1/2 < \varphi_{osm} < 1$ in regime II (eqn (49)) and to $\varphi_{osm} < 1/2$ in regime III (eqn (50)). Fig. 15(a) demonstrates that the osmotic coefficient is inversely proportional to the condensation

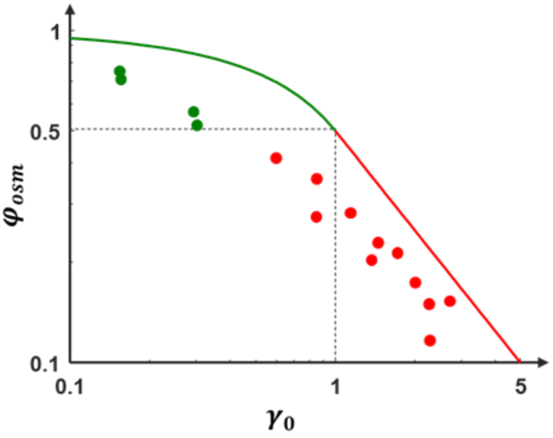

Fig. 16 The theoretical prediction of the dependence of osmotic coefficient on the condensation parameter $\gamma_0 = Z_0 l_B/L$ for the semidilute cylindrical nanoparticles (solid lines – eqn (52)) and the experimental data[24,34,35] for the semidilute flexible polyelectrolytes (solid points). The weak counterion condensation regime I for $\varphi_{osm} > 1/2$ is shown by green points while strong counterion condensation regime III for $\varphi_{osm} < 1/2$ is shown by red points. Both axes are logarithmic.

parameter γ_0 in regime III at constant volume fraction ϕ (eqn (50)). Fig. 15(b) shows that the in regime III ($\gamma_0 = 1.5$ and 3), osmotic coefficient φ_{osm} decreases logarithmically with the increasing volume fraction ϕ at a constant condensation parameter γ_0 (eqn (50)).

The scaling prediction of the osmotic coefficient for semidilute cylindrical particles is calculated from eqn (38) in regime II and eqn (44c) with $\gamma(l_c = R/e) = 1/2$ in regime III using eqn (48):

$$\varphi_{osm} \approx \begin{cases} 1-\dfrac{\gamma_0}{2} & \text{semidilute cylindrical NPs regime II} \\ \dfrac{1}{2\gamma_0} & \text{semidilute cylindrical NPs regime III} \end{cases} \tag{52}$$

The scaling prediction of the osmotic coefficient for the semidilute cylindrical charges (eqn (52)) is sketched in Fig. 16 with green line for $\varphi_{osm} > 1/2$ in regime I and red line for $\varphi_{osm} < 1/2$ in regime III. The experimental data for the osmotic coefficient of flexible polyelectrolytes (solid points in Fig. 16) is in reasonable agreement with the theoretical prediction for semidilute nanorod solution (eqn (52)). The relative horizontal shift of the experimental data with respect to theoretical prediction is related in part to the way the condensation parameter γ_0 is calculated for flexible polyelectrolytes. The condensation parameter was estimated by dividing the product of total valence and Bjerrum length by the fully stretched size of the flexible chain. This underestimates the actual bare condensation parameter, as the fully stretched size of the chain is never achieved even for strongly charged flexible polyelectrolytes. This approximation becomes progressively worse with decreasing condensation parameter by the factor of relative chain extension decreasing from ~2/3 to below ½ of its fully extended size.

5. Summary

We present a scaling model of counterion distribution in low-salt solutions of spherical or cylindrical charged particles. We identify three different regimes depending on particle volume fraction ϕ and the condensation parameter γ_0 defined as the ratio of particle charge valence Z_0 to the number of Bjerrum lengths l_B per particle size ($\gamma_0 = Z_0 l_B / 2r_0$ for spherical particles with radii r_0 defined in eqn (15) or $\gamma_0 = Z_0 l_B / L$ for cylindrical particles with length L defined in eqn (31)). Volume fraction ϕ is defined as the ratio of the physical volume occupied by particles to the total solution volume ($\phi \approx r_0^3/r_{cm}^3$ for spherical nanoparticles, $\phi \approx r_0^2 L / r_{cm}^3$ for dilute cylindrical particles and $\phi \approx r_0^2/R^2$ for semidilute cylindrical particles, where $2r_{cm}$ is the average distance between centers of mass of neighboring particles, while 2R is the average distance between axes of symmetry of neighboring nanorods in semidilute solution).

Regime I. Weakly charged particles with no condensed counterions corresponding to condensation parameter $\gamma_0 < 1$ for spherical particles, $\gamma_0 < -1/\ln(\phi^*)$ for dilute cylindrical particles, and $\gamma_0 < -1/\ln(\phi)$ for semidilute cylindrical particles. In this regime the Gouy-Chapman length l_{GC} is larger than the particle radius r_0. The electrostatic potential energy is smaller than kT and the counterions are free and almost uniformly distributed in solution (see Regime I in Fig. 17).

Regime II. Weak counterion condensation regime with less than half of all counterions condensed corresponding to condensation parameter $1 < \gamma_0 < -\ln(\phi)$ for spherical particles, $-1/\ln(\phi^*) < \gamma_0 < \ln(\phi)/\ln(\phi^*)$ for dilute cylindrical particles and $-1/\ln(\phi) < \gamma_0 < 1$ for semidilute cylindrical particles. We identify three zones around charged particles with qualitatively different counterion distribution profiles (see Regime II in Fig. 17): (1) Condensed counterion zone near the surface of the particles ($x < l_c$). (2) Empty zone (exist for spherical and dilute cylindrical nanoparticles with $\gamma_0 > 1$) with high counterion electrostatic energy (larger than kT) with respect to regions in solution with zero electric field, but with a small fraction of counterions in this zone (see $l_c < x < r_{kT}$ in Fig. 17(a), (b) and (c)). Since the effective charge valence of particles does not vary significantly throughout this empty zone, the spatial dependence of electrostatic potential in this zone is the same as for charged objects of the same symmetry in the absence of counterions (Fig. 1). (3) Free counterion zone is further away from the particles (see $x > r_{kT}$ in Fig. 17). The magnitude of the electrostatic energy of counterions (with respect to regions in solution with zero electric field) in the free zone is smaller than kT.

At $\gamma_0 = 1$, there is no empty zone and $l_c = r_{kT}$ for spherical and dilute cylindrical particles (see Fig. 17). The thickness of the empty zone for the spherical and dilute cylindrical particles increases with the condensation parameter γ_0 as l_c decreases inversely proportional to the condensation parameter γ_0 (eqns (27) and (44)):

$$l_c \approx \frac{r_0}{\gamma_{free}} \approx \begin{cases} r_0/\gamma_0 & \text{regime II} \\ r_0/\gamma^*_{free} & \text{regime IIIb} \end{cases} \tag{53}$$

$$\text{spherical and dilute cylindrical NPs with } \phi < \phi^*/\left[\ln(\phi^*)\right]^2$$

and r_{kT} increases proportional to the condensation parameter γ_0 (eqn (1c)):

$$r_{kT} \approx \begin{cases} Z_0 l_B & \text{regime II} \\ Z^*_{free}(\phi) l_B & \text{regime IIIb} \end{cases} \tag{54}$$

$$\text{spherical and dilute cylindrical NPs with } \phi < \phi^*/\left[\ln(\phi^*)\right]^2$$

Note that there is no empty zone for semidilute cylindrical particles due to the absence of the spherical symmetry zone, which would attract a significant fraction of counterions upon sufficient dilution.

Regime III. Strong counterion condensation regime with most of the counterions condensed corresponding to condensation parameter $\gamma_0 > -\ln(\phi)$ for spherical particles, $\gamma_0 > \ln(\phi)/\ln(\phi^*)$ for dilute cylindrical particles and $\gamma_0 > 1$ for semidilute cylindrical particles. There are two counterion populations for the strong counterion condensation regime III: condensed counterions at distances from particle surface $x = r - r_0 < l_c$ (see eqn (53) for l_c) and free counterions far away from particles in the free counterion zone at distances $r_{kT} < x < r_{cm}$ (eqn (54) for r_{kT}). There are more condensed counterions in regime III than free counterions due to the deeper mean-field single counterion free energy well near the particle (red lines in Fig. 4 and Fig. 9). In spherical particle regime

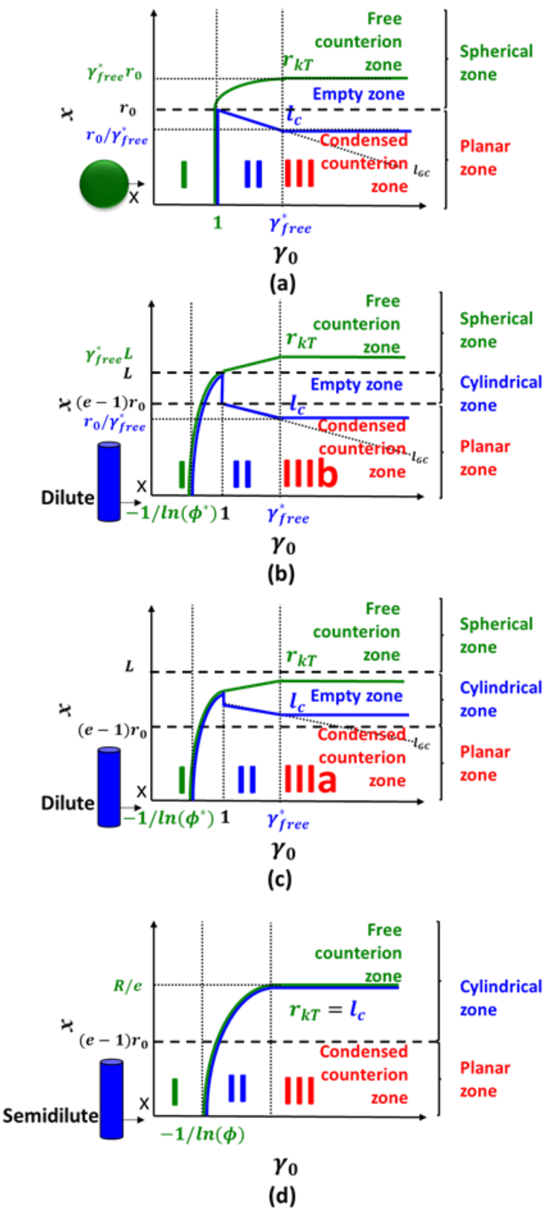

Fig. 17 Length scales of the boundaries between three counterion distribution zones: condensed counterion zone closer to the nanoparticle surface, free counterion zone further away from the nanoparticles, and empty zone in between for (a) spherical nanoparticles , (b) dilute cylindrical nanoparticles with empty cylindrical zone ($\phi < \phi^*/[\ln(\phi^*)]^2$), (c) dilute cylindrical nanoparticles with condensed counterions in cylindrical zone ($\phi^*/[\ln(\phi^*)]^2 < \phi < \phi^*$) and (d) semidilute cylindrical nanoparticles ($\phi > \phi^*$). Blue lines: the thickness of the condensed counterion zone l_c. Green lines: the inner boundary of free counterion zone r_{kT}. The different symmetry zones are separated by the thick dashed lines. All axes are logarithmic.

III and cylindrical particle regime IIIb, the thickness of the condensation layer l_c is larger than Gouy-Chapman length l_{GC} but smaller than the size of the planar zone (see the blue lines in Fig. 17(a) and (b)). The condensed counterions reside in the planar zone described by the Gouy-Chapman solution (eqns (11) and (12)). The inner boundary of free counterion zone r_{kT} in these regimes is larger than r_0 (see the green lines in Fig. 17(a) and (b)) and there is an empty zone with almost no counterions and strongly varying electrostatic potential at distances from the charged surface $l_c < x < r_{kT}$.

In contrast, in semidilute solutions and dilute solutions of cylindrical particles in regime IIIa, the thickness of condensed counterion layer l_c increases with the increasing particle concentration and becomes larger than nanocylinder radius $l_c > (e-1)r_0$ (see the blue lines in Fig. 17(c) and (d)) as the condensed counterions also reside in the cylindrical zone described by the analytical solution[7] (eqns (44) and (45)). The presence of condensed counterions in the cylindrical zone for regime IIIa is due to the detailed balance of the logarithmic entropic and energetic part of free energy there. For the semidilute cylindrical particles, the condensed counterions occupy almost the entire cylindrical zone with the thickness of the condensed counterion zone $l_c \cong R/e$.

The results of this paper could be used to understand the distribution of counterions on different length scales from nanoparticles and its dependence on various physical parameters including particle size and shape, concentration, and valence, and predict the osmotic pressure of the solution based on the free counterion concentration. The results presented in the main part of the paper are for the low salt solutions with the average distance between solute particles smaller than the Debye length. The effect of the added salt is discussed in Appendix D. The distribution of counterions is important for the theories of colloidal stability[28,29], electrophoretic mobility[30], conductivity[31], and viscosity[32,33] of charged particles. This paper primarily focuses on rigid particles and the extension of this work to flexible polymers will be presented in future publications.

Author contributions

QT carried out all numerical calculations, participated in the design of the study and drafted the manuscript. MR conceived and designed the study. Both authors wrote the manuscript.

Conflicts of interest

There are no conflicts of interest to declare.

Appendix A: Examples of parameters for the nanoparticles in different regimes

Table 2 Examples of parameters and length scales of spherical and cylindrical nanoparticles in different regimes.

Regime	Z_0	r_0	r_{cm}	l_B	L	γ_0
Spherical-I	10	10nm	200nm	0.7nm		0.7
Spherical-II	70	5nm	200nm	0.7nm		9.8
Spherical-III	70	5nm	50nm	0.7nm		9.8
Spherical-III	300	5nm	200nm	0.7nm		42
Cylindrical-I	50	10nm	200nm	0.7nm	50nm	0.7
Cylindrical-II	100	10nm	200nm	0.7nm	50nm	1.4
Cylindrical-IIIa	100	10nm	80nm	0.7nm	50nm	1.4
Cylindrical-IIIa	500	10nm	200nm	0.7nm	100nm	3.5
Cylindrical-IIIb	500	30nm	200nm	0.7nm	100nm	3.5

Appendix B: Comparison of the scaling and numerical solutions of the spherical particles

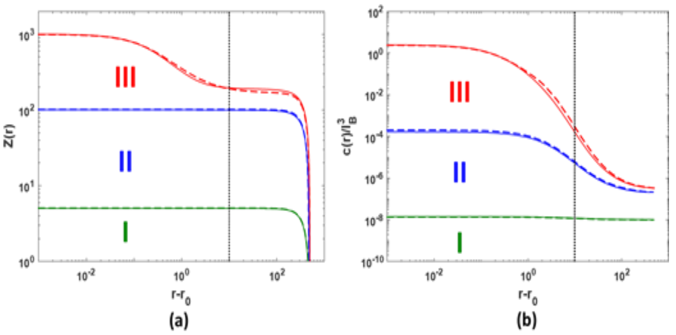

Fig. 18 The comparison of the numerical solutions of the Poisson-Boltzmann equation (solid lines) and the scaling approximations eqns (27) – (29) (dotted lines) for weakly charged spherical particles ($Z_0 = 5$, green), spherical particles with weak counterion condensation ($Z_0 = 100$, blue), and spherical particles with strong counterion condensation ($Z_0 = 1000$, red) with $r_0 = 1$, $l_B = 1$, $r_{cm} = 500$, and $Z_{free} = 3r_0/l_B \ln(r_{cm}/r_0)$ (eqn (29)) for (a) effective charge valence and (b) counterion concentration. All axes are logarithmic.

The comparisons of the effective charge valence and counterion concentration between the numerical solution of the nonlinear Poisson-Boltzmann equation (eqns (19) and (20)) and the scaling solutions (eqns (27), (28), and (29)) for spherical particles in different regimes are shown in Fig. 18(a) and (b) respectively. The scaling estimates (dashed lines in Fig. 18) agree well with the numerical solution of the Poisson-Boltzmann equation (solid lines in Fig. 18).

Appendix C: Semidilute solutions of nanorods with strong counterion condensation: asymptotic limit

The analytical solution of counterion concentration and effective line charge number density is given as[7]

$$c(r)\approx \frac{\beta^2}{2\pi r^2 l_B}\left[\sin\left(\beta\ln(r/\zeta)\right)\right]^{-2} \tag{55}$$

$$\gamma_{eff}(r)\approx 1+\frac{\beta}{\tan\left(\beta\ln(r/\zeta)\right)} \tag{56}$$

where r is the axial distance from the center of the cylindrical nanoparticles (see Fig. 7) and β and ζ are the variables determined by the following boundary conditions at the inner ($r = r_0$) and the outer ($r = R$) boundaries of the cylindrical zone:

$$\tan\left(\beta\ln\frac{r_0}{\zeta}\right)=\frac{\beta}{\gamma_0-1} \tag{57}$$

$$\tan\left(\beta\ln\frac{R}{\zeta}\right)=\frac{\beta}{\gamma_R-1} \tag{58}$$

where γ_R is the effective line charge density at the outer boundary of the cylindrical zone. Note that β can be imaginary if $\gamma_0 \ll 1$ or $\gamma_R \gg 1$. Here we only focus on the solutions with real $\beta > 0$, $\zeta > 0$ and $0 < \beta\ln(r_0/\zeta) < \beta\ln(R/\zeta) < \pi$ without loss of generality for the trigonometric functions. In the limit of large $\ln(R/r_0) \gg \pi$, $\gamma_0 \gg 1$, and $\gamma_R \ll 1$, we have $\beta\ln(r_0/\zeta) \ll \pi$, $\pi - \beta\ln(R/\zeta) \ll \pi$, and $\beta = \pi/\ln(eR/r_0) \ll \pi$, and can approximate the tangent function in eqns (57) and (58) by the value of its argument to get:

$$\begin{gathered}\beta=\frac{\pi}{\ln(eR/r_0)}\\ \ln\frac{r}{\zeta}\approx\ln\frac{r}{r_0}+\frac{1}{\gamma_0-1}\approx\frac{\pi}{\beta}+\ln\frac{r}{R}-1\end{gathered} \tag{59}$$

The counterion concentration and the effective charge line number density are then expressed as:

$$c(r)\approx\frac{1}{2\pi r^2 l_B}\frac{\pi^2}{\left[\ln eR/r_0\right]^2}\left[\sin\left(\pi\frac{\ln r/r_0+1/(\gamma_0-1)}{\ln eR/r_0}\right)\right]^{-2} \tag{60}$$

$$\gamma_{eff}(r)\approx 1+\frac{\pi}{\ln eR/r_0}\left[\tan\left(\pi\frac{\ln r/r_0+1/(\gamma_0-1)}{\ln eR/r_0}\right)\right]^{-1} \tag{61}$$

As shown in Fig. 13 and eqn (60), the counterion distribution converges to the asymptotic profile independent of γ_0 at high γ_0:

$$\lim_{\gamma_0\to\infty} c(r)\approx\frac{1}{2\pi r^2 l_B}\frac{\pi^2}{\left[\ln eR/r_0\right]^2}\left[\sin\left(\pi\frac{\ln r/r_0}{\ln eR/r_0}\right)\right]^{-2} \tag{62}$$

The counterion concentration c(r) is roughly proportional to $1/(2\pi r^2 l_B)$, but eqn (62) indicates that c(r) deviates from this simple power-law scaling by the r-dependent factor:

$$\lim_{\gamma_0\to\infty} 2\pi r^2 l_B c(r)\approx\frac{\pi^2}{\left[\ln eR/r_0\right]^2}\left[\sin\left(\pi\frac{\ln r/r_0}{\ln eR/r_0}\right)\right]^{-2} \tag{63}$$

This asymptotic deviation from the power law is plotted in Fig. 13 by the dashed line. The analytical solution of $2\pi r^2 l_B c(r)$ (derived from eqn (60)) approaches this asymptotic “correction factor” with increasing condensation parameter γ_0. At the geometric mean between the inner ($r = er_0$) and the outer ($r = R$) boundaries of the cylindrical zone, sin(π/2)=1 and the deviation from the reciprocal square power-law dependence of the asymptotic c(r) reaches the maximum factor of $\pi^2/[\ln(e R/r_0)]^2$.

Since the effective mean-field single counterion free energy difference in the cylindrical zone is $\Delta F_{eff}(r,R) = -2kT\ln(r/R) + e\Delta\psi(r,R) \approx -kT\ln(c(r)/c(R))$, the numerical solution shows that the free energy difference $\Delta F_{eff}(r,R)$ becomes independent of γ_0 for $R \gg r > er_0$ and $\gamma_0 \gg 1$ and this effective single counterion mean-field free energy $\Delta F_{eff}(r_0,R)$ near the surface decreases with the increasing linear charge density γ_0, resulting in an increasing number of condensed counterions in this potential well (see Fig. 13). The asymptotic effective line charge number density is obtained from eqn (61).

$$\lim_{\gamma_0\to\infty}\gamma_{eff}(r)\approx 1+\frac{\pi}{\ln eR/r_0}\left[\tan\left(\pi\frac{\ln r/r_0}{\ln eR/r_0}\right)\right]^{-1} \qquad (64)$$

Appendix D: Effect of added salt on counterion distribution in solutions of nanoparticles with strong counterion condensation

In this section, we present a scaling description of counterion distributions in solutions of spherical and cylindrical nanoparticles in strong counterion condensation regime with added salt. These solutions contain both monovalent co-ions with the same sign of charge as nanoparticles and monovalent counterions with the opposite sign of charge. We do not distinguish between counterions and salt ions with the same sign of charge. The addition of salt to the solution of charged nanoparticles has two effects on the distribution of counterions: on one hand, the salt ions screen the electrostatic interaction beyond the Debye length r_D (see eqn (13)): both the effective charge valence and the electric field decay exponentially at distance from nanoparticles larger than the Debye length r_D. On the other hand, the entropic part of chemical potential at r_D (eqn (8)) varies logarithmically with salt concentration (eqn (13)). The increase of salt concentration has a qualitatively similar effect on counterion distribution at $x < r_D$ to the increase of the counterion concentration with decreasing separation between the particles ($2r_{cm}$ in the dilute case or 2R in the semidilute nanorod case) in salt-free solutions (eqn (8)). Both of these ways of increasing counterion concentration result in the increase of the entropic part of the counterion free energy at the solution location with zero electric field. The electrostatic interactions are unscreened on length scales shorter than Debye length and counterion distribution for $x < r_D$ in solutions with added salt can be approximated by the salt-free counterion distribution with the separation between the particles (r_{cm} or R) replaced by r_D. Depending on the magnitude of Debye length r_D relative to the separation between particles (r_{cm} or R) and particle size ($2r_0$ and L), we identify the following salt regimes: (i) low salt regime with $r_D > r_{cm}$ for spherical and dilute cylindrical particles and $r_D > R$ for semidilute cylindrical particles; (ii) intermediate salt regime with screening in the spherical zone ($r_0 < r_D < r_{cm}$ for spherical charged particles and $L < r_D < r_{cm}$ for dilute cylindrical particles); (iii) high salt regime with screening in the cylindrical zone ($r_0 < r_D < L$ for dilute cylindrical particles and $r_0 < r_D < R$ for semidilute cylindrical particles); and (iv) ultra-high salt regime with screening in the planar zone ($r_D < r_0$). The dependences of the effective charge valence Z(x) and the counterion concentration $c_+(x)$ on the distance x from the particle surface in solutions of spherical and cylindrical particles of different ionic strength corresponding to the above salt regimes are sketched in Fig. 19 and Fig. 20 respectively. These dependences on length scales shorter than Debye length were obtained from the corresponding salt-free cases.

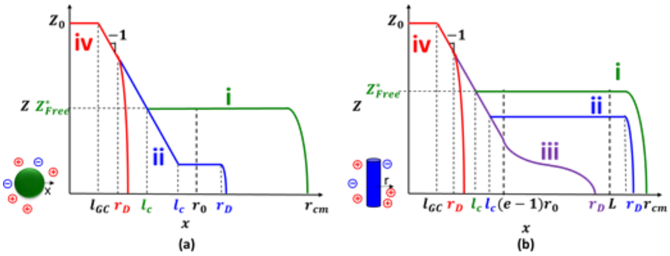

Fig. 19 Effective charge valence Z(x) for (a) spherical particles and (b) dilute cylindrical particles in strong counterion condensation regime III at different salt concentration regimes: (i) low salt regime with $r_D > r_{cm}$ (green lines) for dilute solutions; (ii) intermediate salt regime with $r_0 < r_D < r_{cm}$ for dilute spherical and $L < r_D < r_{cm}$ for dilute cylindrical particles (blue lines). (iii) high salt regime for cylindrical particles with $r_0 < r_D < R$ (purple lines) and (iv) ultra-high salt regime with $r_D < r_0$ (red lines). The effective charge valence Z(x) in low salt regime (i) was approximated by the effective charge valence in the dilute salt-free case (red line in Fig. 6(a) and Fig. 10(a)). The effective charge valence Z(x) for $x < r_D$ in the intermediate salt regime (ii) was estimated by the effective charge valence in the dilute salt-free solutions by replacing the separation between particles r_{cm} by the Debye length r_D (red line in Fig. 6(a) and red or brown line in Fig. 10(a) depending on value of r_D). The effective line charge number density γ(x) in the high salt regime (iii) was approximated by γ(x) in the semidilute salt-free solutions by substituting R with r_D (red line in Fig. 10(b)). The effective charge valence Z(x) for $x < r_D$ in ultra-high salt regime (iv) with screening in the planar zone was approximated by the salt-free Gouy-Chapman solution (Fig. 2(c)) with the full Gouy-Chapman analytical solution for the counterion distribution near a charged plane in the presence of salt presented in the literature[1,2,3]. All axes are logarithmic.

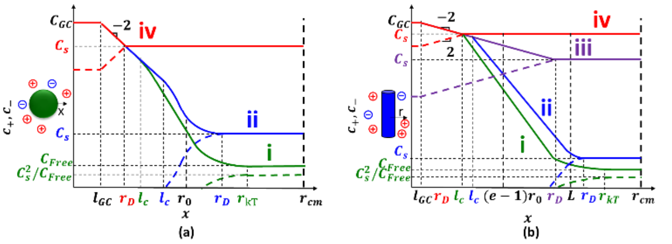

Fig. 20 Counterion concentration $c_+(x)$ (solid lines) and co-ion concentration $c_-(x)$ (dashed lines) for (a) spherical particles and (b) dilute cylindrical particles in strong counterion condensation regime III with different regimes of salt concentrations: (i) low salt regime with $r_D > r_{cm}$ (green lines). (ii) intermediate salt regime (blue lines), and (iii) high salt regime (purple lines), and (iv) ultra-high salt regime (red lines). The counterion concentration in the low salt regime (i) was approximated by the counterion concentration in dilute salt-free case (red line in Fig. 6(b) and Fig. 11(a)). The counterion concentration for $x<r_D$ in the intermediate salt regimes (ii) can be approximated by the counterion concentration profile in the dilute salt-free solution by replacing the separation between particles r_{cm} by the Debye length r_D (red line in Fig. 6(b) and red or brown line in Fig. 11(a) depending on value of r_D). The counterion concentration for $x<r_D$ in the high salt regime (iii) was estimated by c(x) in the semidilute salt-free case by replacing R with r_D (red line in Fig. 11(b)). The counterion concentration for $x<r_D$ in the ultra-high salt regime (iv) can be approximated by the salt-free Gouy-Chapman solution (Fig. 2(d)) with the full analytical solution presented in the literature[1,2,3]. The co-ion concentration $c_-(x)$ is inversely proportional to the counterion concentration $c_+(x)$ with $c_+(x)c_-(x) = c_s^2$. All axes are logarithmic.

Acknowledgements

The authors thank Ralph Colby for many helpful discussions. M. R. acknowledges financial support from National Science Foundation under Grant EFMA-1830957 and the National Institutes of Health under Grant P01-HL108808.

References

1 M. Gouy, *J. Phys. Théorique Appliquée*, 1910, **9**, 457–468.

2 D. L. Chapman, *London, Edinburgh, Dublin Philos. Mag. J. Sci.*, 1913, **25**, 475–481.

3 D. Andelman, *Handb. Biol. Phys.*, 1995, **1**, 603–642.

4 D. Andelman, *Soft Condens. matter Phys. Mol. cell Biol.*, 2006, **6**, 97–135.

5 R. M. Fuoss, A. Katchalsky and S. Lifson, *Proc. Natl. Acad. Sci. U. S. A.*, 1951, **37**, 579.

6 G. S. Manning, *J. Chem. Phys.*, 1969, **51**, 924–933.

7 A. Deshkovski, S. Obukhov and M. Rubinstein, *Phys. Rev. Lett.*, 2001, **86**, 2341–2344.

8 B. H. Zimm and M. Le Bret, *J. Biomol. Struct. Dyn.*, 1983, **1**, 461–471.

9 S. Alexander, P. M. Chaikin, P. Grant, G. J. Morales, P. Pincus and D. Hone, *J. Chem. Phys.*, 1984, **80**, 5776–5781.

10 G. V. Ramanathan, *J. Chem. Phys.*, 1988, **88**, 3887–3892.

11 L. Belloni, *Colloids Surfaces A Physicochem. Eng. Asp.*, 1998, **140**, 227–243.

12 D. A. J. Gillespie, J. E. Hallett, O. Elujoba, A. F. Che Hamzah, R. M. Richardson and P. Bartlett, *Soft Matter*, 2014, **10**, 566–577.

13 R. Kjellander and S. Marcělja, *Chem. Phys. Lett.*, 1984, **112**, 49–53.

14 O. Stern, *Zeitschrift für Elektrochemie und Angew. Phys. Chemie*, 1924, **30**, 508–516.

15 T. Markovich, D. Andelman and R. Podgornik, *EPL (Europhysics Lett.*, 2016, **113**, 26004.

16 Y. Avni, T. Markovich, R. Podgornik and D. Andelman, *Soft Matter*, 2018, **14**, 6058–6069.

17 I. Rouzina and V. A. Bloomfield, *J. Phys. Chem.*, 1996, **100**, 9977–9989.

18 V. I. Perel and B. I. Shklovskii, *Phys. A Stat. Mech. its Appl.*, 1999, **274**, 446–453.

19 B. I. Shklovskii, *Phys. Rev. Lett.*, 1999, **82**, 3268–3271.

20 A. V. Dobrynin, A. Deshkovski and M. Rubinstein, *Macromolecules*, 2001, **34**, 3421–3436.

21 J. Kamcev, D. R. Paul, G. S. Manning and B. D. Freeman, *Macromolecules*, 2018, **51**, 5519–5529.

22 E. Huckel and P. Debye, *Phys. Z*, 1923, **24**, 185–206.

23 M. Rubinstein and R. H. Colby, *Polymer physics*, Oxford university press New York, 2003, vol. 23.

24 G. S. Manning, *J. Chem. Phys.*, 1969, **51**, 924–933.

25 S. Lifson and A. Katchalsky, *Biophys. Other Top.*, 1976, **13**, 49–61.

26 The corresponding volume fraction is estimated from the balance of electrostatic energy change in the cylindrical zone $|e\Delta\psi(r_0, L)| \approx 2\gamma_0 kT\ln(L/r_0) \approx 4kT\ln(L/r_0)$ (eqn (34)) and entropic free energy change $|\Delta F_s(r_0, L)| \approx kT\ln(c(r_0)/c(L)) \approx kT\ln\left((r_0^2 l_B)^{-1}/(L/r_{cm}^3 l_B)\right) \approx kT\ln\left(r_{cm}^3/(Lr_0^2)\right)$ (eqns (8) and (32)) to be $\phi < \phi^{*2}$.

27 Q. Liao, A. V. Dobrynin and M. Rubinstein, *Macromolecules*, 2003, **36**, 3399–3410.

28 J. DufrÊChe, T. O. White and J. Hansen, *Mol. Phys.*, 2003, **101**, 1741–1759.

29 L. Ehrl, Z. Jia, H. Wu, M. Lattuada, M. Soos and M. Morbidelli, *Langmuir*, 2009, **25**, 2696–2702.

30 F. Carrique, E. Ruiz-Reina, F. J. Arroyo, M. L. Jiménez and Á. V. Delgado, *Langmuir*, 2008, **24**, 2395–2406.

31 G. S. Manning, *J. Phys. Chem.*, 1981, **85**, 1506–1515.

32 F. J. Rubio-Hernández, F. Carrique and E. Ruiz-Reina, *Adv. Colloid Interface Sci.*, 2004, 107, 51–60.

33 H. Ohshima, *Colloid Polym. Sci.*, 2020, **298**, 1551–1557.

34 W. Kern, *Z. Phys. Chem. A*, 1939, **184**, 197–210.

35 Z. Alexandrowicz, *J. Polym. Sci.*, 1959, **40**, 91–106.